Contents lists available at ScienceDirect

Chaos, Solitons and Fractals

journal homepage: www.elsevier.com/locate/chaos

Pattern dynamics of a harvested predator–prey model

Mengxin Chen [a], Seokjun Ham [b], Yongho Choi [c], Hyundong Kim [d], Junseok Kim [b],*

[a] *College of Mathematics and Information Science, Henan Normal University, Xinxiang 453007, China*
[b] *Department of Mathematics, Korea University, Seoul 02841, Republic of Korea*
[c] *Department of Computer & Information Engineering, Daegu University, Gyeongsan-si, Gyeongsangbuk-do 38453, Republic of Korea*
[d] *Department of Mathematics and Physcis, Gangneung-Wonju National University, Gangneung 25457, Republic of Korea*

ARTICLE INFO

ABSTRACT

This paper investigates the pattern dynamics of a harvested predator–prey model with no-flux boundary conditions. Firstly, we analyze the positive equilibrium types of the local temporal model. We find that they can be classified as nodes, foci, or centers depending on the harvesting coefficient within a certain parameter range. Furthermore, the direction of the Hopf bifurcation is determined by employing the first Lyapunov coefficient. In the subsequent analysis, we present the conditions for the existence of Turing instability and classify the different pattern selections using amplitude equations with the assistance of weakly nonlinear analysis by treating the harvesting coefficient as a critical parameter. Finally, the spot patterns and mixed patterns are respectively displayed in 2D space, on spherical and torus surfaces with various harvesting coefficient values. Especially, we can numerically demonstrate that the diffusion rate of the prey population will strongly affect the pattern structures of the model. These results can provide a reference for understanding the interaction dynamics of the model.

1. Introduction

Patterns exist broadly in the real world due to the movement of substances, providing valuable information for understanding the dynamic properties of natural phenomena. For example, they contribute to the understanding of formation mechanisms of animal body surface patterns, the distribution of savannah vegetation, disease propagation, and more. The spatial pattern theory in reaction–diffusion equations was originally proposed by Turing in his influential work [1] regarding the chemical basis of morphogenesis. Since then, pattern formation has been extensively studied in various fields such as chemistry, biology, ecology, and epidemiology. Li and Zhou [2] investigated the dynamics of a general Selkov–Schnakenberg reaction–diffusion model for global stability and Hopf bifurcation. By choosing the diffusion coefficient as the critical parameter for Turing instability, Han et al. [3] obtained the conditions under which Turing instability occurs and provided amplitude equations that allow for the classification of various patterns. Sarker and Sahani [4] reported Turing patterns in both 2D and 3D regions, establishing a relationship between the wavenumber and the superdiffusive exponent of the Turing pattern using an SI epidemic model with standard incidence rate and superdiffusion effect. Dolnik et al. [5] investigated the impact of obstructions on the growth of Turing patterns, offering new insights into biological pattern growth

and formation through the Lengyel–Epstein reaction–diffusion model. Chang et al. [6] examined the pattern formation of a delayed predator–prey model in a network environment, specifically highlighting wave patterns in deterministic and random networks. For further publications on pattern formation, we recommend consulting references such as [7–15].

It is evident that predation is widespread in the natural environment, and we have a particular interest in studying the pattern dynamics of predator–prey models. In this context, we consider a dimensionless reaction–diffusion version of the predator–prey model, expressed as follows:

$$
\begin{cases}
\dfrac{\partial u}{\partial t} = d_1 \Delta u + u(1-u) - \dfrac{au^2 w}{u^2 + bw^2}, \\
\dfrac{\partial w}{\partial t} = d_2 \Delta w + \gamma w \left(1 - \dfrac{w}{u}\right),
\end{cases}
$$

where $u = u(\mathbf{x}, t)$ and $w = w(\mathbf{x}, t)$ represent the densities of the prey and predators at location $\mathbf{x}$ and time t, respectively. Here, Δ is the Laplacian operator, and d_1 and d_2 are the diffusion rates of the prey u and predators w, separately. The positive constants γ, b, and a have specific interpretations in the context of the model. The nonlinear term $\frac{au^2}{u^2+bw^2}$ is known as the ratio-dependent Holling III type functional response [16], and the term $\frac{w}{u}$ is the Leslie–Gower term [17].

It is noticed that the development and utilization of natural resources have become global concerns. Therefore, it is imperative to ensure the scientific management of biological resource development.

In fact, owing to commercial and economic interests, the exploitation of biological resources and species harvesting are common strategies, and implementing effective harvesting policies can protect overfished populations from possible extinction [18]. On the other hand, numerous studies have explored the dynamic behavior of species interaction models incorporating harvesting effect. Omari et al. [19] investigated the dynamics of a stage-structured predator–prey model with distributed maturation delay and a harvesting term. They demonstrated that the dynamics of a stage-structured predator–prey model heavily depend on the harvesting efforts. Jiang et al. [20] analyzed the stability of equilibrium, the existence of Turing instability, and global Hopf bifurcation in the zooplankton population and a Holling III functional response. They also demonstrated that the unstable interval of the positive equilibrium decreases with increasing harvesting effort. Xiao [21] reported the effect of seasonal harvesting on population survival using a model with constant-yield harvesting. The results indicate that the ecological system exhibits persistence with seasonal constant-yield harvesting. Additional references such as [22–29] provide further dynamic results of ecological models incorporating harvesting terms. However, it is worth noting that there is limited existing literature reporting the dynamical behaviors of the above predator–prey model in the presence of harvesting effects. Accordingly, motivated by the discussions above, we consider the following predator–prey model with a harvesting term:

$$
\begin{cases}
\dfrac{\partial u}{\partial t} = d_1 \Delta u + u(1-u) - \dfrac{au^2 w}{u^2 + bw^2} - H_1, \\[2mm]
\dfrac{\partial w}{\partial t} = d_2 \Delta w + \gamma w(1 - \dfrac{w}{u}) - H_2,
\end{cases}
\tag{1}
$$

where H_1 implies harvesting of the prey population, and H_2 denotes harvesting of the predator population. It is important to note that different types of harvesting can be chosen for H_1 and H_2. For instance, the constant-yield harvesting (cf. [22,23]) can be represented by $H_1 = h_1$ and $H_2 = h_2$, where h_1 and h_2 are positive constants. The linear harvesting (cf. [24,25,30]) corresponds to $H_1 = h_1 u$ and $H_2 = h_2 w$. The quadratic harvesting (cf. [26,27]) is given by $H_1 = q_1 E_1 u^2$ and $H_2 = q_2 E_2 w^2$, where q_1 and q_2 are the catchability coefficients of populations u and w, and E_1 and E_2 represent the external efforts devoted to harvesting populations u and w, respectively. Nonlinear harvesting (cf. [28,29]) is described by $H_1 = \dfrac{q_1 E_1 u}{c_1 E_1 + l_1 u}$ and $H_2 = \dfrac{q_2 E_2 w}{c_2 E_2 + l_2 w}$, where q_1 and q_2 represent the catchability coefficients of prey u and predator w, and E represents the external effort devoted to harvesting. Furthermore, $c_1, c_2, l_1,$ and l_2 are positive constants. Typically, the term $\dfrac{q_1 E_1 u}{c_1 E_1 + l_1 u}$ (or $\dfrac{q_2 E_2 u}{c_2 E_2 + l_2 u}$) is referred to as a Michaelis–Menten type functional response, originally proposed by Clark [31] in the 1970s.

Let us review some known results regarding the model (1). In the absence of harvesting ($H_1 = H_2 = 0$), the stability of the equilibrium, pattern formation near the Turing bifurcation, and Turing–Hopf bifurcation were analyzed in [32]. The concepts of uniform persistence, global attractors, and asymptotic stability of the positive equilibrium were considered in [33]. The boundedness of classical solutions, the existence of codimension-two Turing–Hopf points (C2THP) and the analysis of amplitude equations near C2THP were discussed in [34]. In the case where $H_1 = 0$ and $H_2 = h_2 w$, the boundedness of solutions and the nonexistence of nonconstant steady states for the continuous version of the model were considered in [24]. Additionally, the existence and direction of the Hopf bifurcation in a network environment were demonstrated. Notably, the case of predator harvesting was considered in [24]. However, the dynamics of the model (1) with prey harvesting were not studied. To address this, we set $H_1 = Hu$ ($H > 0$) and

$H_2 = 0$ in the model (1), resulting in the following predator–prey model incorporating prey harvesting:

$$
\begin{cases}
\dfrac{\partial u}{\partial t} = d_1 \Delta u + u(1-u) - \dfrac{au^2 w}{u^2 + bw^2} - Hu, & \mathbf{x} \in \Omega, \ t > 0, \\[2mm]
\dfrac{\partial w}{\partial t} = d_2 \Delta w + \gamma w(1 - \dfrac{w}{u}), & \mathbf{x} \in \Omega, \ t > 0, \\[2mm]
\dfrac{\partial u}{\partial \nu} = \dfrac{\partial w}{\partial \nu} = 0, & \mathbf{x} \in \partial\Omega, \ t \geq 0, \\[2mm]
u(\mathbf{x}, 0) = u_0(\mathbf{x}) \geq 0, \quad w(\mathbf{x}, 0) = w_0(\mathbf{x}) \geq 0, & \mathbf{x} \in \Omega,
\end{cases}
\tag{2}
$$

where $\Omega \subset \mathbb{R}^N$ with $N \geq 1$ is a bounded domain, and ν is the outward unit normal vector along the smooth boundary $\partial\Omega$. The initial densities of populations u and w are defined by $u_0(\mathbf{x}) \geq 0$ and $w_0(\mathbf{x}) \geq 0$, respectively, indicating that they are non-negative.

Pattern dynamics play an important role in understanding the complex interaction dynamics among the species of a spatial ecological mathematical model for population dynamics. In this study, our focus is on the pattern dynamics of the predator–prey model (2) incorporating the harvesting effect. A natural question arises: how does the harvesting effect impact the dynamic profiles of the diffusive model (1)? We aim to answer this question theoretically and numerically. Specifically, when certain conditions are satisfied (i.e., $0 < H < 1 - \frac{a}{1+b}$ and $0 < a < 1 + b$), model (2) possesses a unique positive equilibrium $E_* = (u_*, w_*) = \left(1 - H - \frac{a}{1+b}, 1 - H - \frac{a}{1+b}\right)$. However, if these conditions are not met, the positive equilibrium E_* does not exist. Furthermore, we observe that the positive equilibrium E_* undergoes a transition from a stable node to a stable focus, followed by an unstable focus and an unstable node, eventually reaching a center as the harvesting constant H varies.

Additionally, the harvesting constant H governs the existence of the Hopf bifurcation and the Turing instability. By selecting the harvesting constant H as the critical value for the Turing instability, we discover a variety of spatial patterns emerging in model (2). Numerical simulations reveal that different spatial patterns emerge as the harvesting constant H changes. Importantly, these findings are also confirmed on spherical and torus surfaces. These theoretical and numerical results convincingly demonstrate the significant role played by the harvesting effect in this predator–prey model, leading to complex dynamic behaviors. Throughout the entire paper, the novelty of this study mainly includes two aspects. Theoretically, the harvesting effect is introduced in the model, and we can show that the harvesting coefficient can induce the Hopf bifurcation and Turing instability of the model (2). Numerically, we can observe the complicated patterns on the spherical surface and torus surface by considering the Laplace–Beltrami operator. These results broaden the investigation of the predator–prey model (2) with the harvesting effect.

The paper is organized as follows. In Section 2, we analyze the dynamics of the local temporal model (2), including stability analysis, the Hopf bifurcation, and its direction. In Section 3, we derive the amplitude equations near the threshold to investigate various pattern selections. In Section 4, we perform pattern simulations of model (2) using numerical schemes. Finally, we conclude the article in Section 5.

2. Dynamics of the local model

Firstly, let us describe some dynamic behaviors of the temporal model with reference to (2). The model is presented below.

$$
\begin{cases}
\dfrac{du}{dt} = u(1-u) - \dfrac{au^2 v}{u^2 + bw^2} - Hu, \\[2mm]
\dfrac{dw}{dt} = \gamma w(1 - \dfrac{w}{u}).
\end{cases}
\tag{3}
$$

Denote by $f(u, w) = u(1-u) - \frac{au^2 v}{u^2 + bw^2} - Hu$ and $g(u, w) = \gamma w(1 - \frac{w}{u})$. To obtain the positive equilibrium, denoted as $E_* = (u_*, w_*)$, of the model (3), we set $f(u, w) = g(u, w) = 0$. By solving these equations, one obtains $E_* = (u_*, w_*) = \left(1 - H - \frac{a}{1+b}, 1 - H - \frac{a}{1+b}\right)$ for $0 < H < 1 - \frac{a}{1+b}$

and $0 < a < 1+b$. Now, we can obtain the Jacobian matrix, denoted as J_0, of the system (3) at E_* as shown below.

$$J_0 = \begin{pmatrix} H - H_0 & \delta \\ \gamma & -\gamma \end{pmatrix},$$

where $H_0 = 1 - \frac{2a}{(1+b)^2}$ and $\delta = \frac{a(b-1)}{(1+b)^2}$. As such, the characteristic equation at equilibrium E_* is read as follows:

$$\lambda^2 - T_0(H)\lambda + D_0(H) = 0, \tag{4}$$

where $T_0(H) = H - H_0 - \gamma$ and $D_0(H) = \gamma(H_0 - H - \delta) = \gamma u_* > 0$. We establish the following result.

Theorem 2.1. *Suppose that* $0 < a < 1+b, 0 < H < 1 - \frac{a}{1+b}$ *and* $H_0 + \gamma > 0$ *are valid.*

(i) If $0 < H \le H_0 + \gamma - 2\sqrt{\gamma u_*}$, *then* E_* *is a node, and it is locally asymptotically stable.*

(ii) If $H_0 + \gamma - 2\sqrt{\gamma u_*} < H < H_0 + \gamma$, *then* E_* *is a focus, and it is locally asymptotically stable;*

(iii) If $H_0 + \gamma < H < H_0 + \gamma + 2\sqrt{\gamma u_*}$, *then* E_* *is a focus, and it is unstable.*

(iv) If $H \ge H_0 + \gamma + 2\sqrt{\gamma u_*}$, *then* E_* *is a node, and it is unstable.*

(v) If $H = H_0 + \gamma$, *then* E_* *is a center, and there is a Hopf bifurcation.*

Proof. Owing to $D_0(H) = \gamma u_* > 0$, the stability of the positive equilibrium E_* only depends on the sign of $T_0(H)$. This means that the positive equilibrium E_* is locally asymptotically stable when $0 < H < H_0 + \gamma$, while it is unstable for $H > H_0 + \gamma$. In the sequel, we denote by $\Gamma = T_0^2(H) - 4D_0(H)$. By computation, we have $\Gamma = T_0^2(H) - 4D_0(H) = (H - H_0 - \gamma - 2\sqrt{\gamma u_*})(H - H_0 - \gamma + 2\sqrt{\gamma u_*})$. Thus, we have the following cases with respect to the sign of Γ and stability of E_*.

Case I. $0 < H \le H_0 + \gamma - 2\sqrt{\gamma u_*}$.

If $0 < H \le H_0 + \gamma - 2\sqrt{\gamma u_*}$ is true, we immediately have $\Gamma \ge 0$. In this case, the characteristic Eq. (4) has two real eigenvalues with negative real parts. Therefore, the positive equilibrium E_* is a node, and it is locally asymptotically stable.

Case II. $H_0 + \gamma - 2\sqrt{\gamma u_*} < H < H_0 + \gamma$.

For this case, it is easy to check that $H - H_0 - \gamma - 2\sqrt{\gamma u_*} < 0$ and $H - H_0 - \gamma + 2\sqrt{\gamma u_*} > 0$ are fulfilled. This means that $\Gamma < 0$ is true. We infer that the characteristic Eq. (4) has a pair of conjugate complex eigenvalues with negative real parts. Consequently, the positive equilibrium E_* is a focus, and it is locally asymptotically stable.

Case III. $H_0 + \gamma < H < H_0 + \gamma + 2\sqrt{\gamma u_*}$.

For this case, it is easy to check that $H - H_0 - \gamma - 2\sqrt{\gamma u_*} < 0$ and $H - H_0 - \gamma + 2\sqrt{\gamma u_*} > 0$ are fulfilled. This means that $\Gamma < 0$ is true. We infer that the characteristic Eq. (4) has a pair of conjugate complex eigenvalues with positive real parts. Consequently, the positive equilibrium E_* is a focus, and it is unstable.

Case IV. $H \ge H_0 + \gamma + 2\sqrt{\gamma u_*}$.

For this case, $\Gamma \ge 0$ is valid. Moreover, we have $H_0 + \gamma + 2\sqrt{\gamma u_*} > H_0 + \gamma$. This implies that the characteristic Eq. (4) has two real eigenvalues with positive real parts. Therefore, the positive equilibrium E_* is a node and it is unstable.

Case V. If $H = H_0 + \gamma$, we know that $T_0(H) = 0$. Accordingly, the characteristic Eq. (4) has a pair of purely imaginary eigenvalues, namely, E_* is a center. In addition, we find $\frac{d Re(\lambda)}{dH}\big|_{H=H_0+\gamma} = \frac{1}{2} > 0$. Thus, the model (3) undergoes the Hopf bifurcation at $H = H_0 + \gamma$. We conclude the proof.

Remark 2.1. Based on Theorem 2.1, we observe that E_* undergoes the transition from a stable node to a stable focus, then to an unstable focus, and finally to an unstable node, as well as a center, with changes in the harvesting constant H. This illustrates that the harvesting constant H can affect the dynamic profiles of the model (3).

Remark 2.2. We will perform numerical simulations to confirm the validity of statements (i) and (ii) in Theorem 2.1. To this end, we fix the

parameters as follows: $a = 0.5$, $b = 1$, and $\gamma = 0.5$. Then, we calculate $H_0 + \gamma - 2\sqrt{\gamma u_*} = 0.4754$, $H_0 + \gamma = 1.25$, and $H_0 + \gamma + 2\sqrt{\gamma u_*} = 2.0246$. By choosing the harvesting constant $H = 0.47$, our numerical simulation shows that $E_* = (0.28, 0.28)$ is a stable node, as depicted in Fig. 1(a). Hence, statement (i) of Theorem 2.1 is true. Next, we consider $a = 0.5, b = 0.5$, and $\gamma = 0.045$. In this case, we have $H_0 + \gamma - 2\sqrt{\gamma u_*} = 0.4831$, $H_0 + \gamma = 0.6006$, and $H_0 + \gamma + 2\sqrt{\gamma u_*} = 0.7180$. By choosing the harvesting constant $H = 0.59$, our numerical experiments indicate that the unique positive equilibrium $E_* = (0.0767, 0.0767)$ is a stable focus, as shown in Fig. 1(b). Therefore, statement (ii) of Theorem 2.1 is true. Overall, the theoretical predictions presented in Theorem 2.1 are valid, as confirmed by our numerical simulations.

Note that when $H = H_0 + \gamma$, the model (3) exhibits a Hopf bifurcation. The following result pertains to the direction of the Hopf bifurcation.

Theorem 2.2. *Suppose that* $0 < a < 1 + b, 0 < H < 1 - \frac{a}{1+b}$, *and* $H = H_0 + \gamma > 0$. *Then, the Hopf bifurcation is supercritical (resp. subcritical) when* $L_1 < 0$ *(resp.* $L_1 > 0$*). Moreover, the periodic solution bifurcated from the Hopf bifurcation is stable (resp. unstable) when* $L_1 < 0$ *(resp.* $L_1 > 0$*), where* L_1 *can be found below.*

Proof. Let $\widetilde{u} = u - u_*$ and $\widetilde{w} = w - w_*$. We will continue to denote $\widetilde{u}$ and $\widetilde{w}$ as u and w, respectively. Then, model (3) is approximately equivalent to the following system:

$$\begin{cases} \frac{du}{dt} = f_u u + f_w w + f_{uu} u^2 + f_{uw} uw + f_{ww} w^2 + f_{uuu} u^3 \\ \quad + f_{uuw} u^2 w + f_{uww} uw^2 + f_{www} w^3 + \mathcal{O}(|u, w|^4), \\ \frac{dw}{dt} = g_u u + g_w w + g_{uu} u^2 + g_{uw} uw + g_{ww} w^2 + g_{uuu} u^3 \\ \quad + g_{uuw} u^2 w + g_{uww} uw^2 + g_{www} w^3 + \mathcal{O}(|u, w|^4), \end{cases}$$

where $\mathcal{O}(|u, w|^4)$ are higher terms and

$$f_u = H - H_0, \quad f_w = \frac{a(b-1)}{(1+b)^2}, \quad g_u = \gamma, \quad g_w = -\gamma,$$

$$f_{uu} = \frac{ab(3-b)}{u_*(1+b)^3} - 1, \quad f_{uw} = \frac{2ab(b-3)}{u_*(1+b)^3}, \quad g_{uw} = \frac{2\gamma}{u_*},$$

$$f_{uuw} = \frac{ab(b^2 - 14b + 9)}{u_*^2(1+b)^4},$$

$$g_{uu} = -\frac{\gamma}{u_*}, \quad g_{uuu} = \frac{\gamma}{u_*^2}, \quad g_{uuw} = -\frac{2\gamma}{u_*^2}, \quad f_{uuu} = \frac{4ab(b-1)}{u_*^2(1+b)^4},$$

$$f_{uww} = \frac{2ab(8b - b^2 - 3)}{u_*^2(1+b)^4},$$

$$f_{ww} = \frac{ab(3-b)}{u_*(1+b)^3}, \quad f_{www} = \frac{ab(b^2 - 6b + 1)}{u_*^2(1+b)^4}, \quad g_{uww} = \frac{\gamma}{u_*^2},$$

$$g_{ww} = -\frac{\gamma}{u_*}, \quad g_{www} = 0.$$

To obtain the discriminant of the direction of the Hopf bifurcation, we need to compute the following first Lyapunov number.

$$\begin{aligned} L_1 = & \frac{-3\pi}{2 f_w D_0(H)^{3/2}} \{ [f_u g_u (f_{uw}^2 + f_{uw} g_{ww} + f_{ww} g_{uw}) \\ & + f_u f_w (g_{uw}^2 + f_{uu} g_{uw} + f_{uw} g_{ww}) \\ & + g_u^2 (f_{uw} f_{ww} + 2 f_{ww} g_{ww}) - 2 f_u g_u (g_{ww}^2 - f_{uu} f_{ww}) \\ & - 2 f_u f_w (f_{uu}^2 - g_{uu} g_{ww}) \\ & - f_w^2 (2 g_{uu} f_{uu} + g_{uu} g_{uu}) + (f_w g_u - 2 f_u^2)(g_{uw} g_{ww} - f_{uw} f_{uu})] \\ & - (f_u^2 + f_w g_u)[3(g_u g_{www} - f_w f_{uuu}) + 2 f_u (f_{uuw} + g_{uww}) \\ & + (g_u f_{uww} - f_w g_{uuw})] \}. \end{aligned}$$

At the critical point of Hopf bifurcation, $H = H_0 + \gamma$, we obtain

$$\begin{aligned} L_1 = & \frac{-3\pi}{2 f_w'(\gamma u_*)^{3/2}} \{ [4 f_u' g_u' f_{ww}'(f_{ww}' - g_{ww}') + 2 f_u' f_w' g_{ww}'(2 g_{ww}' - f_{ww}' - 1) \\ & + 2(g_u^2)' f_{ww}'(-f_{ww}' + g_{ww}') - 2 f_u' g_u'((g_{ww}^2)' - f_{uu}' f_{ww}') \end{aligned}$$
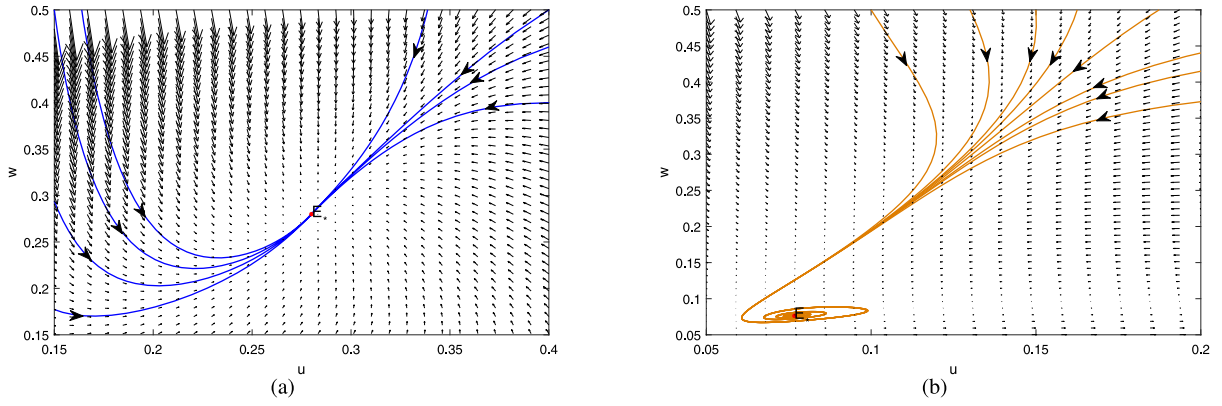
Fig. 1. The phase portraits of the model (3) in the plane of $u - w$. (a): the unique positive equilibrium $E_* = (0.28, 0.28)$ is a stable node with the parameters $a = 0.5, b = 1, \gamma = 0.5$, and $H = 0.47$; (b): the unique positive equilibrium $E_* = (0.0767, 0.0767)$ is a stable focus when choosing the parameters $a = 0.5, b = 0.5, \gamma = 0.045$, and $H = 0.59$.
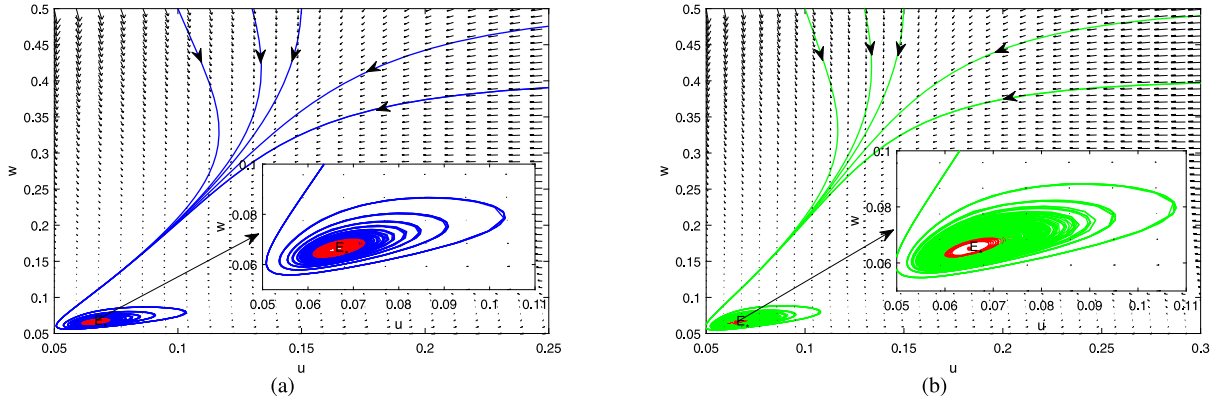

Fig. 2. Stable periodic solutions emerge in the model (3). (a): Taking $a = 0.5, b = 0.5, \gamma = 0.045$, and $H = 0.6006$; (b): Choosing the parameter $a = 0.5, b = 0.5, \gamma = 0.046$, and $H = 0.6016$.

$$
\begin{aligned}
& - 2 f_u' f_w'((f_{uu}^2)' - (g_{ww}^2)') \\
& - (f_w^2)'(2g_{ww}' f_{uu}' - 2(g_{ww}^2)') + (f_w' g_u' - 2(f_u^2)')(-2(g_{ww}^2)' + 2f_{ww}' f_{uu}')] \\
& - ((f_u^2)' + f_w' g_u')[2f_u'(f_{uuw}' + g_{uww}') - 3f_w' f_{uuu}' \\
& + (g_u' f_{uww}' - f_w' g_{uuw}')]\},
\end{aligned}
$$

where $\mathcal{P}'$ denotes the evaluation of $\mathcal{P} = \mathcal{P}\big|_{H=H_0+\gamma}$. In light of [35], we know that the Hopf bifurcation is supercritical (resp. subcritical) when $L_1 < 0$ (resp. $L_1 > 0$). Moreover, the periodic solution bifurcated from the Hopf bifurcation is stable (resp. unstable) when $L_1 < 0$ (resp. $L_1 > 0$). This concludes the proof.

Remark 2.3. Taking the parameters $a = 0.5, b = 0.5$, and $\gamma = 0.045$, we obtain the critical value of the Hopf bifurcation as $H_0 + \gamma = 0.6006$. Consequently, when $H = 0.6006$, we have $L_1 = -9.5557E + 03 < 0$. According to Theorem 2.2, we conclude that model (3) undergoes a supercritical Hopf bifurcation, which is confirmed by our numerical simulation as shown in Fig. 2(b). Similarly, if we choose $a = 0.5, b = 0.5$, and $\gamma = 0.046$, we obtain the Hopf bifurcation critical value $H_0 + \gamma = 0.6016$. Setting $H = 0.6016$, we find $L_1 = -1.0145E + 04 < 0$. Our numerical simulation demonstrates the emergence of a stable periodic solution in model (3) due to the supercritical Hopf bifurcation.

3. Turing instability

3.1. Existence conditions

Now, let us explore the conditions for the occurrence of Turing instability around the positive equilibrium E_* of model (2). We can obtain a linearized form of model (2) as follows:

$$
\frac{\partial \mathbf{U}}{\partial t} = J\mathbf{U} + D\Delta\mathbf{U}, \tag{5}
$$

where

$$
\mathbf{U} = \begin{pmatrix} u - u_* \\ w - w_* \end{pmatrix}, \quad D = \begin{pmatrix} d_1 & 0 \\ 0 & d_2 \end{pmatrix}, \quad J = \begin{pmatrix} H - H_0 & \delta \\ \gamma & -\gamma \end{pmatrix}.
$$

For Eq. (5), we consider the following general form solution:

$$
\mathbf{U} = \begin{pmatrix} a_k \\ b_k \end{pmatrix} e^{\lambda t + i\mathbf{k}\cdot\mathbf{r}},
$$

where λ is the growth rate of perturbation at time t, $\mathbf{k} = (k_x, k_y)$ is the wave vector, and it gives $k = |\mathbf{k}|$, $\mathbf{r} = (x, y)$ represents the spatial vector in 2D space, i admits $i^2 = -1$, $a_k \neq 0$ and $b_k \neq 0$ are constants. By direct calculation, we can obtain the dispersion equation as follows:

$$
\lambda^2 - T_k(H)\lambda + D_k(H) = 0, \tag{6}
$$

where

$$
\begin{cases}
T_k(H) = -(d_1 + d_2)k^2 + H - H_0 - \gamma, \\
D_k(H) = d_1 d_2 k^4 + [\gamma d_1 - (H - H_0)d_2]k^2 + D_0(H).
\end{cases}
$$

Obviously, $D_k(H) > 0$ for all $k \neq 0$ when $H \leq H_0$. For the Turing instability, we should first guarantee that the unique positive equilibrium E_* is locally asymptotically stable for the temporal model (3). Therefore, one of the conditions (i) and (ii) of Theorem 2.1 should be fulfilled. It is clear that we only need to restrict $0 < H < H_0 + \gamma$ to be valid. Secondly, the unique positive equilibrium E_* will lose its stability as the diffusion effect is introduced. This indicates that we need require $D_k(H) < 0$ for certain $k \neq 0$ and $T_k(H) < 0$ for any $k \neq 0$. In fact, $T_k(H) < 0$ can be immediately satisfied because the condition

$0 < H < H_0 + \gamma$ holds true. Therefore, the next task is to determine under what condition $D_k(H) < 0$ for certain $k \neq 0$ is also valid. To this end, consider the following marginal stability condition

$$\min(D_{k_c^2}(H)) = 0, \tag{7}$$

where k_c^2 is the critical wave number of the Turing instability and is undetermined. In light of (7), one has

$$\Theta(H) := d_2^2 H^2 - 2d_2(\gamma d_1 + H_0 d_2)H + (\gamma d_1 + H_0 d_2)^2 - 4d_1 d_2 D_0(H) = 0,$$

and $\min(D_{k_c^2}(H)) = -\Theta(H)$. An easy computation shows that the root's existence discriminant of $\Theta(H) = 0$ is $16 d_1 d_2^3 D_0(H) > 0$. Next, for the convenience of discussion, we always assume that $H_0 > 0$. Choosing the harvesting constant H as the threshold of Turing instability, we proceed as follows.

Case I. $(\gamma d_1 + H_0 d_2)^2 - 4d_1 d_2 D_0(H) > 0$.

For this case, it is easy to infer that $\Theta(H) = 0$ has two distinct positive real roots

$$H_1^c = \frac{\gamma d_1 + H_0 d_2 - 2\sqrt{d_1 d_2 D_0(H)}}{d_2},$$

$$H_2^c = \frac{\gamma d_1 + H_0 d_2 + 2\sqrt{d_1 d_2 D_0(H)}}{d_2}.$$

We infer that $\Theta(H) > 0$ as $0 < H < H_1^c$ or $H > H_2^c$, and $\Theta(H) < 0$ as $H_1^c < H < H_2^c$. It is noticed that $\min(D_{k_c^2}(H)) = -\Theta(H)$, so there exists a certain $k = k_c$ such that $D_k(H) < 0$ if $0 < H < H_1^c$ or $H > H_2^c$ and $D_k(H) > 0$ if $H_1^c < H < H_2^c$. Recalling the necessary condition $0 < H < H_0 + \gamma$, we can conclude that the unique positive equilibrium E_* is locally asymptotically stable when $H_1^c < H < \min\{H_2^c, H_0 + \gamma\}$, while it becomes unstable when $0 < H < \min\{H_1^c, H_0 + \gamma\}$ or $H_0 + \gamma > H > H_2^c$. Consequently, the diffusive model (2) may suffer from the Turing instability when $0 < H < \min\{H_1^c, H_0 + \gamma\}$ or $H_0 + \gamma > H > H_2^c$.

Case II. $(\gamma d_1 + H_0 d_2)^2 - 4d_1 d_2 D_0(H) \leq 0$.

For this case, $\Theta(H) = 0$ only has a positive real root

$$H_3^c = \frac{\gamma d_1 + H_0 d_2 + 2\sqrt{d_1 d_2 D_0(H)}}{d_2}.$$

Clearly, $\Theta(H) > 0$ as $H > H_3^c$, and $\Theta(H) < 0$ when $0 < H < H_3^c$. Hence, there exists a certain $k = k_c$ such that $D_k(H) < 0$ if $H > H_3^c$ and $D_k(H) > 0$ if $0 < H < H_3^c$. We conclude that the unique positive equilibrium E_* is locally asymptotically stable for $0 < H < \min\{H_3^c, H_0 + \gamma\}$ and it becomes unstable for $H_0 + \gamma > H > H_3^c$. In this case, Turing instability appears only when $H_0 + \gamma > H > H_3^c$.

Now, let us determine the critical wave number k_c. Using Eq. (7) once again, we find that $k_c = \sqrt[4]{\frac{D_0(H)}{d_1 d_2}}$. It is evident that k_c uniquely depends on the diffusion coefficients d_1, d_2, and $D_0(H)$.

In summary, we establish the following result.

Theorem 3.1. *Suppose that $0 < a < 1 + b, 0 < H < 1 - \frac{a}{1+b}$, and $H_0 > 0$. We have*

(i) if $(\gamma d_1 + H_0 d_2)^2 - 4d_1 d_2 D_0(H) > 0$, then the unique positive equilibrium E_* is locally asymptotically stable when $H_1^c < H < \min\{H_2^c, H_0 + \gamma\}$, and it is unstable when $0 < H < \min\{H_1^c, H_0 + \gamma\}$ or $H_0 + \gamma > H > H_2^c$. Moreover, the diffusive model (2) may exhibit Turing instability when $0 < H < \min\{H_1^c, H_0 + \gamma\}$ or $H_0 + \gamma > H > H_2^c$, with the critical wave number $k_c = \sqrt[4]{\frac{D_0(H)}{d_1 d_2}}$;

(ii) if $(\gamma d_1 + H_0 d_2)^2 - 4d_1 d_2 D_0(H) \leq 0$, then the unique positive equilibrium E_* is locally asymptotically stable when $0 < H < \min\{H_3^c, H_0 + \gamma\}$, and it becomes unstable when $H_0 + \gamma > H > H_3^c$. Furthermore, Turing instability appears in the model (2) when $H_0 + \gamma > H > H_3^c$ with the critical wave number $k_c = \sqrt[4]{\frac{D_0(H)}{d_1 d_2}}$.

Remark 3.1. To better understand Theorem 3.1, we plot the stability diagram in the $\gamma - H$ plane, see Fig. 3. The parameter plane is divided

into four domains, namely I, II, III, and IV. Now, let us explain Fig. 3(a). In domain I, we have $H > H_0 + \gamma$. This indicates that the unique positive equilibrium E_* is unstable in the temporal model (3). Therefore, this domain is classified as a non-Turing domain. Upon crossing the critical curve of Hopf bifurcation at $H = H_0 + \gamma$ and entering domain II, we have $H_2^c < H < H_0 + \gamma$. We claim that the unique positive equilibrium E_* is locally asymptotically stable in model (3), while it remains unstable in model (2). Consequently, this is referred to as the Turing domain. Moving into domain III, we find $H_1^c < H < H_2^c$ and $H_1^c < H < H_0 + \gamma$. Consequently, this domain is considered stable. In fact, it is a bistable domain because the unique positive equilibrium E_* is locally asymptotically stable in both models (2) and (3). Finally, upon crossing the critical curve of Turing instability at H_1^c and entering domain IV, we observe that $0 < H < H_1^c$. This also represents a Turing domain. We can provide a similar explanation for Fig. 3(b). Here, Fig. 3(a) and (b) correspond to (i) and (ii) of Theorem 3.1, respectively.

We have confirmed the existence of the Turing instability, which could be induced by the harvesting constant H. In the following sections, we assume that model (2) exhibits Turing instability at the threshold $H = H_c$, where H_c could be H_1^c, H_2^c, or H_3^c with different assumptions. Our task now is to deduce the amplitude equation around the onset of Turing instability at $H = H_c$. The main method we used here is weakly nonlinear analysis, as described in Refs. [7,9,28] and the reference cited therein. This technique is useful to helping us classify the pattern selection.

3.2. Amplitude equation

Let us rewrite the reaction–diffusion model (2) at E_* as follows:

$$\frac{\partial \mathbf{U}}{\partial t} = \mathbf{L}\mathbf{U} + \mathbf{N}(\mathbf{U}, \mathbf{U}), \tag{8}$$

where

$$\mathbf{U} = \begin{pmatrix} u \\ w \end{pmatrix}, \quad \mathbf{L} = \begin{pmatrix} H - H_0 + d_1\Delta & \delta \\ \gamma & -\gamma + d_2\Delta \end{pmatrix},$$

and

$$\mathbf{N} = \begin{pmatrix} f_{uu}u^2 + f_{uw}uw + f_{ww}w^2 + f_{uuu}u^3 \\ +f_{uuw}u^2w + f_{uww}uw^2 + f_{www}w^3 \\ g_{uu}u^2 + g_{uw}uw + g_{ww}w^2 + g_{uuu}u^3 \\ +g_{uuw}u^2w + g_{uww}uw^2 + g_{www}w^3 \end{pmatrix} + \mathcal{O}(4).$$

Now, around the onset of Turing instability at $H = H_c$, let

$$H - H_c = \varepsilon H_1 + \varepsilon^2 H_2 + \varepsilon^3 H_3 + \mathcal{O}(4). \tag{9}$$

Constructing time scale transformations $T_0 = t, T_1 = \varepsilon t, T_2 = \varepsilon^2 t$ and $T_3 = \varepsilon^3 t$, we have

$$\frac{\partial}{\partial t} = \frac{\partial}{\partial T_0} + \varepsilon \frac{\partial}{\partial T_1} + \varepsilon^2 \frac{\partial}{\partial T_2} + \varepsilon^3 \frac{\partial}{\partial T_3} + \mathcal{O}(4). \tag{10}$$

Expanding the solution $\mathbf{U}$ as follows

$$\mathbf{U} = \begin{pmatrix} u \\ w \end{pmatrix} = \varepsilon \begin{pmatrix} u_1 \\ w_1 \end{pmatrix} + \varepsilon^2 \begin{pmatrix} u_2 \\ w_2 \end{pmatrix} + \varepsilon^3 \begin{pmatrix} u_3 \\ w_3 \end{pmatrix} + \mathcal{O}(4). \tag{11}$$

For the nonlinear term $\mathbf{N}$, we set

$$\mathbf{N} = \varepsilon^2 \mathbf{N}_2 + \varepsilon^3 \mathbf{N}_3 + \mathcal{O}(\varepsilon^4), \tag{12}$$

with

$$\mathbf{N}_2 = \begin{pmatrix} f_{uu}u_1^2 + f_{uw}u_1 w_1 + f_{ww}w_1^2 \\ g_{uu}u_1^2 + g_{uw}u_1 w_1 + g_{ww}w_1^2 \end{pmatrix},$$

and

$$\mathbf{N}_3 = \begin{pmatrix} 2f_{uu}u_1 u_2 + f_{uw}(u_1 w_2 + u_2 w_1) + 2f_{ww}w_1 w_2 \\ +f_{uuu}u_1^3 + f_{uuw}u_1^2 w_1 + f_{uww}u_1 w_1^2 + f_{www}w_1^3 \\ 2g_{uu}u_1 u_2 + g_{uw}(u_1 w_2 + u_2 w_1) + 2g_{ww}w_1 w_2 \\ +g_{uuu}u_1^3 + g_{uuw}u_1^2 w_1 + g_{uww}u_1 w_1^2 + g_{www}w_1^3 \end{pmatrix}.$$
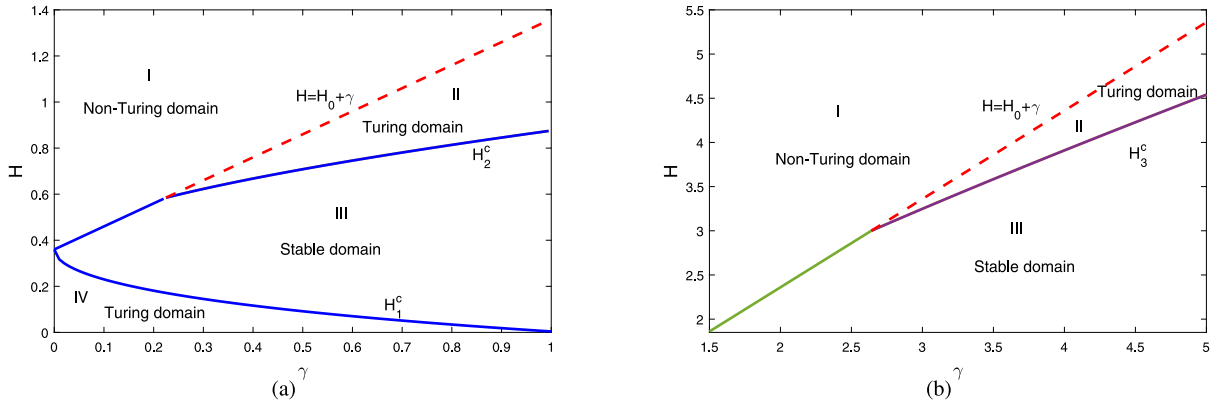
Fig. 3. Stability diagrams in $\gamma - H$ planes, where figure (a) for case (i) and figure (b) for case (ii) in Theorem 3.1, respectively.

Finally, expanding the operator $\mathbf{L}$ as belows:

$$\mathbf{L} = \mathbf{L}_c + (H - H_c)\mathbf{M}, \tag{13}$$

where

$$\mathbf{L}_c = \begin{pmatrix} H_c - H_0 + d_1\Delta & \delta \\ \gamma & -\gamma + d_2\Delta \end{pmatrix}, \quad \mathbf{M} = \begin{pmatrix} 1 & 0 \\ 0 & 0 \end{pmatrix}.$$

Accordingly, substituting Eqs. (9)–(13) into Eq. (8) results in

$\mathcal{O}(\varepsilon)$:

$$\mathbf{L}_c \begin{pmatrix} u_1 \\ w_1 \end{pmatrix} = \mathbf{0}. \tag{14}$$

$\mathcal{O}(\varepsilon^2)$:

$$\mathbf{L}_c \begin{pmatrix} u_2 \\ w_2 \end{pmatrix} = \frac{\partial}{\partial T_1} \begin{pmatrix} u_1 \\ w_1 \end{pmatrix} - H_1\mathbf{M} \begin{pmatrix} u_1 \\ w_1 \end{pmatrix} - \mathbf{N}_2. \tag{15}$$

$\mathcal{O}(\varepsilon^3)$:

$$\mathbf{L}_c \begin{pmatrix} u_3 \\ w_3 \end{pmatrix} = \frac{\partial}{\partial T_1} \begin{pmatrix} u_2 \\ w_2 \end{pmatrix} + \frac{\partial}{\partial T_2} \begin{pmatrix} u_1 \\ w_1 \end{pmatrix}$$
$$- H_1\mathbf{M} \begin{pmatrix} u_2 \\ w_2 \end{pmatrix} - H_2\mathbf{M} \begin{pmatrix} u_1 \\ w_1 \end{pmatrix} - \mathbf{N}_3. \tag{16}$$

For the perturbation Eq. (14), consider the following general solution

$$\begin{pmatrix} u_1 \\ w_1 \end{pmatrix} = \begin{pmatrix} \phi \\ 1 \end{pmatrix} \left(\sum_{j=1}^{3} A_j \exp(i\mathbf{k}_j \cdot \mathbf{r}) + \sum_{j=1}^{3} \bar{A}_j \exp(-i\mathbf{k}_j \cdot \mathbf{r}) \right), \tag{17}$$

where $\phi = \frac{\delta}{d_1 k_c^2 + H_0 - H_c}$, $|\mathbf{k}_j| = k_c = \sqrt[4]{\frac{D_0}{d_1 d_2}}$ and A_j are the amplitudes with respect to the mode of $\exp(i\mathbf{k}_j \cdot r)$. In what follows, let $\mathbf{L}_c^*$ be the adjoint operator of $\mathbf{L}_c$ and

$$\begin{pmatrix} 1 \\ \varphi \end{pmatrix} (\exp(-i\mathbf{k}_j \cdot \mathbf{r})) + c.c., \quad j = 1, 2, 3, \tag{18}$$

with $\varphi = \frac{d_1 k_c^2 + H_0 - H}{\gamma}$ be the zero eigenvector of the adjoint operator $\mathbf{L}_c^*$. Moreover, we define

$$\begin{pmatrix} H_u \\ H_w \end{pmatrix} \triangleq \frac{\partial}{\partial T_1} \begin{pmatrix} u_1 \\ w_1 \end{pmatrix} - H_1\mathbf{M} \begin{pmatrix} u_1 \\ w_1 \end{pmatrix} - \mathbf{N_2}.$$

In light of the orthogonality condition to the perturbation Eq. (15), we have

$$(1, \varphi)\exp(-i\mathbf{k}_j \cdot \mathbf{r}) \begin{pmatrix} H_u^j \\ H_w^j \end{pmatrix} = 0, \quad j = 1, 2, 3, \tag{19}$$

where H_u^j and H_w^j are the coefficients corresponding to $\exp(i\mathbf{k}_j \cdot \mathbf{r})$ in H_u and H_w, respectively. We can obtain

$$\begin{cases} (\phi + \varphi)\dfrac{\partial A_1}{\partial T_1} = \phi H_1 A_1 + 2(h_1 + \varphi h_2)\bar{A}_2\bar{A}_3, \\ (\phi + \varphi)\dfrac{\partial A_2}{\partial T_1} = \phi H_1 A_2 + 2(h_1 + \varphi h_2)\bar{A}_1\bar{A}_3, \\ (\phi + \varphi)\dfrac{\partial A_3}{\partial T_1} = \phi H_1 A_3 + 2(h_1 + \varphi h_2)\bar{A}_1\bar{A}_2, \end{cases} \tag{20}$$

where $h_1 = f_{uu}\phi^2 + f_{uw}\phi + f_{ww}$, $h_2 = g_{uu}\phi^2 + g_{uw}\phi + g_{ww}$. In what follows, let us substitute Eq. (17) into Eq. (15), we get

$$\begin{pmatrix} u_2 \\ w_2 \end{pmatrix} = \begin{pmatrix} U_0 \\ W_0 \end{pmatrix} + \sum_{j=1}^{3} \begin{pmatrix} U_j \\ W_j \end{pmatrix} e^{i\mathbf{k}_j \cdot \mathbf{r}}$$
$$+ \sum_{j=1}^{3} \begin{pmatrix} U_{jj} \\ W_{jj} \end{pmatrix} e^{2i\mathbf{k}_j \cdot \mathbf{r}} + \begin{pmatrix} U_{12} \\ W_{12} \end{pmatrix} e^{i(\mathbf{k_1}-\mathbf{k_2})\cdot \mathbf{r}}$$
$$+ \begin{pmatrix} U_{23} \\ W_{23} \end{pmatrix} e^{i(\mathbf{k_2}-\mathbf{k_3})\cdot \mathbf{r}} + \begin{pmatrix} U_{31} \\ W_{31} \end{pmatrix} e^{i(\mathbf{k_3}-\mathbf{k_1})\cdot \mathbf{r}} + c.c., \tag{21}$$

where

$$U_j = \phi W_j, \quad \begin{pmatrix} U_0 \\ W_0 \end{pmatrix} = \begin{pmatrix} u_{00} \\ w_{00} \end{pmatrix}(|A_1|^2 + |A_2|^2 + |A_3|^2),$$

$$\begin{pmatrix} U_{jj} \\ W_{jj} \end{pmatrix} = \begin{pmatrix} u_{11} \\ w_{11} \end{pmatrix} A_j^2, \quad \begin{pmatrix} U_{12} \\ W_{12} \end{pmatrix} = \begin{pmatrix} u_{22} \\ w_{22} \end{pmatrix} A_1\bar{A}_2,$$

$$\begin{pmatrix} U_{23} \\ W_{23} \end{pmatrix} = \begin{pmatrix} u_{22} \\ w_{22} \end{pmatrix} A_2\bar{A}_3, \quad \begin{pmatrix} U_{31} \\ W_{31} \end{pmatrix} = \begin{pmatrix} u_{22} \\ w_{22} \end{pmatrix} A_3\bar{A}_1,$$

with

$$\begin{pmatrix} u_{00} \\ w_{00} \end{pmatrix} = \begin{pmatrix} \dfrac{2(\delta h_2 + \gamma h_1)}{\gamma(H_0 - H_c - \delta)} \\ \dfrac{2[\gamma h_1 - (H_c - H_0)h_2]}{\gamma(H_0 - H_c - \delta)} \end{pmatrix},$$

$$\begin{pmatrix} u_{11} \\ w_{11} \end{pmatrix} = \begin{pmatrix} \dfrac{\delta h_2 + (\gamma + 4d_2 k_c^2)h_1}{[(H_c - H_0 - 4d_1 k_c^2)(-\gamma - 4d_2 k_c^2) - \gamma\delta]} \\ \dfrac{\gamma h_1 - (H_c - H_0 - 4d_1 k_c^2)h_2}{[(H_c - H_0 - 4d_1 k_c^2)(-\gamma - 4d_2 k_c^2) - \gamma\delta]} \end{pmatrix},$$

$$\begin{pmatrix} u_{22} \\ w_{22} \end{pmatrix} = \begin{pmatrix} \dfrac{2[\delta h_2 + (\gamma + 3d_2 k_c^2)h_1]}{[(H_c - H_0 - 3d_1 k_c^2)(-\gamma - 3d_2 k_c^2) - \gamma\delta]} \\ \dfrac{2[\gamma h_1 - (H_c - H_0 - 3d_1 k_c^2)h_2]}{[(H_c - H_0 - 3d_1 k_c^2)(-\gamma - 3d_2 k_c^2) - \gamma\delta]} \end{pmatrix}.$$

Now, let $(R_u, R_v)^T$ denote the right-hand side of Eq. (16). By substituting Eqs. (17) and (21) into Eq. (16), we can obtain $(R_u^j, R_v^j)^T$

corresponding to $e^{i\mathbf{k}_j \cdot \mathbf{r}}$. This represents

$$
\begin{cases}
R_u^1 = \phi \dfrac{\partial W_1}{\partial T_1} + \phi \dfrac{\partial A_1}{\partial T_2} - \phi H_1 W_1 - \phi H_2 A_1 \\
\qquad - 2h_1(\bar{A}_2 \bar{W}_3 + \bar{A}_3 \bar{W}_2) - (c_1|A_1|^2 + c_2(|A_2|^2 + |A_3|^2)) A_1, \\
R_v^1 = \dfrac{\partial W_1}{\partial T_1} + \dfrac{\partial A_1}{\partial T_2} - 2h_2(\bar{A}_2 \bar{W}_3 + \bar{A}_3 \bar{W}_2) \\
\qquad - (c_3|A_1|^2 + c_4(|A_2|^2 + |A_3|^2)) A_1, \\
R_u^2 = \phi \dfrac{\partial W_2}{\partial T_1} + \phi \dfrac{\partial A_2}{\partial T_2} - \phi H_1 W_2 - \phi H_2 A_2 \\
\qquad - 2h_1(\bar{A}_1 \bar{W}_3 + \bar{A}_3 \bar{W}_1) - (c_1|A_2|^2 + c_2(|A_1|^2 + |A_3|^2)) A_2, \\
R_v^2 = \dfrac{\partial W_2}{\partial T_1} + \dfrac{\partial A_2}{\partial T_2} - 2h_2(\bar{A}_1 \bar{W}_3 + \bar{A}_3 \bar{W}_1) \\
\qquad - (c_3|A_2|^2 + c_4(|A_1|^2 + |A_3|^2)) A_2, \\
R_u^3 = \phi \dfrac{\partial W_3}{\partial T_1} + \phi \dfrac{\partial A_3}{\partial T_2} - \phi H_1 W_3 - \phi H_2 A_3 \\
\qquad - 2h_1(\bar{A}_1 \bar{W}_2 + \bar{A}_2 \bar{W}_1) - (c_1|A_3|^2 + c_2(|A_1|^2 + |A_2|^2)) A_3, \\
R_v^3 = \dfrac{\partial W_3}{\partial T_1} + \dfrac{\partial A_3}{\partial T_2} - 2h_2(\bar{A}_1 \bar{W}_2 + \bar{A}_2 \bar{W}_1) \\
\qquad - (c_3|A_3|^2 + c_4(|A_1|^2 + |A_2|^2)) A_3,
\end{cases}
$$

with

$$
\begin{cases}
c_1 = (2\phi f_{uu} + f_{uw})(u_{00} + u_{11}) + (\phi f_{uw} + 2f_{ww})(w_{00} + w_{11}) \\
\qquad + 3\phi^3 f_{uuu} + 3\phi^2 f_{uuw} + 3\phi f_{uww} + 3f_{www}, \\
c_2 = (2\phi f_{uu} + f_{uw})(u_{00} + u_{22}) + (\phi f_{uw} + 2f_{ww})(w_{00} + w_{22}) \\
\qquad + 6\phi^3 f_{uuu} + 6\phi^2 f_{uuw} + 6\phi f_{uww} + 6f_{www}, \\
c_3 = (2\phi g_{uu} + g_{uw})(u_{00} + u_{11}) + (\phi g_{uw} + 2g_{ww})(w_{00} + w_{11}) \\
\qquad + 3\phi^3 g_{uuu} + 3\phi^2 g_{uuw} + 3\phi g_{uww} + 3g_{www}, \\
c_4 = (2\phi g_{uu} + g_{uw})(u_{00} + u_{22}) + (\phi g_{uw} + 2g_{ww})(w_{00} + w_{22}) \\
\qquad + 6\phi^3 g_{uuu} + 6\phi^2 g_{uuw} + 6\phi g_{uww} + 6g_{www}.
\end{cases}
$$

If perturbation Eq. (16) has the nontrivial solution $(R_u, R_w)^T$, it must be orthogonal with the zero eigenvectors of $\mathbf{L}_c^*$. This implies that the following condition

$$
(1, \varphi)\exp(-i\mathbf{k}_j \cdot \mathbf{r}) \begin{pmatrix} R_u^j \\ R_w^j \end{pmatrix} = 0, \quad j = 1, 2, 3, \tag{22}
$$

should be fulfilled. Performing direct computations yields

$$
\begin{cases}
(\phi + \varphi)\left(\dfrac{\partial W_1}{\partial T_1} + \dfrac{\partial A_1}{\partial T_2}\right) = \phi(H_1 W_1 + H_2 A_1) \\
\qquad + 2(h_1 + \varphi h_2)(\bar{A}_2 \bar{W}_3 + \bar{A}_3 \bar{W}_2) \\
\qquad + [(c_1 + \varphi c_3)|A_1|^2 \\
\qquad + (c_2 + \varphi c_4)(|A_2|^2 + |A_3|^2)]A_1, \\
(\phi + \varphi)\left(\dfrac{\partial W_2}{\partial T_1} + \dfrac{\partial A_2}{\partial T_2}\right) = \phi(H_1 W_2 + H_2 A_2) \\
\qquad + 2(h_1 + \varphi h_2)(\bar{A}_1 \bar{W}_3 + \bar{A}_3 \bar{W}_1) \\
\qquad + [(c_1 + \varphi c_3)|A_2|^2 \\
\qquad + (c_2 + \varphi c_4)(|A_1|^2 + |A_3|^2)]A_2, \\
(\phi + \varphi)\left(\dfrac{\partial W_3}{\partial T_1} + \dfrac{\partial A_3}{\partial T_2}\right) = \phi(H_1 W_3 + H_2 A_3) \\
\qquad + 2(h_1 + \varphi h_2)(\bar{A}_2 \bar{W}_1 + \bar{A}_1 \bar{W}_2) \\
\qquad + [(c_1 + \varphi c_3)|A_3|^2 \\
\qquad + (c_2 + \varphi c_4)(|A_2|^2 + |A_1|^2)]A_3.
\end{cases} \tag{23}
$$

Considering the perturbation of the amplitude as follows

$$
C_j = \varepsilon A_j + \varepsilon^2 W_j + \mathcal{O}(3).
$$

As a result, by using Eqs. (10), (20) and (23), we can deduce

$$
\begin{cases}
\tau \dfrac{\partial C_1}{\partial t} = \mu C_1 + h \bar{C}_2 \bar{C}_3 - [g_1|C_1|^2 + g_2(|C_2|^2 + |C_3|^2)] C_1, \\
\tau \dfrac{\partial C_2}{\partial t} = \mu C_2 + h \bar{C}_1 \bar{C}_3 - [g_1|C_2|^2 + g_2(|C_1|^2 + |C_3|^2)] C_2, \\
\tau \dfrac{\partial C_3}{\partial t} = \mu C_3 + h \bar{C}_1 \bar{C}_2 - [g_1|C_3|^2 + g_2(|C_1|^2 + |C_2|^2)] C_3,
\end{cases} \tag{24}
$$

where

$$
\mu = \frac{H - H_c}{H_c}, \quad \tau = \frac{\phi + \varphi}{\phi H_c},
$$

$$
h = \frac{2(h_1 + \varphi h_2)}{\phi H_c}, \quad g_1 = -\frac{c_1 + \varphi c_3}{\phi H_c}, \quad g_2 = -\frac{c_2 + \varphi c_4}{\phi H_c}.
$$

Now, suppose that each amplitude in (24) takes the form

$$
C_j = \xi_j \exp(i\theta_j), \quad j = 1, 2, 3, \tag{25}
$$

where ξ_j and θ_j represent the mode and the corresponding phase angle, respectively. Then, we have

$$
\begin{cases}
\tau \dfrac{\partial \theta}{\partial t} = -h \dfrac{\xi_1^2 \xi_2^2 + \xi_1^2 \xi_3^2 + \xi_2^2 \xi_3^2}{\xi_1 \xi_2 \xi_3} \sin \theta, \\
\tau \dfrac{\partial \xi_1}{\partial t} = \mu \xi_1 + h \xi_2 \xi_3 \cos \theta - g_1 \xi_1^3 - g_2(|\xi_2|^2 + |\xi_3|^2)\xi_1, \\
\tau \dfrac{\partial \xi_2}{\partial t} = \mu \xi_2 + h \xi_1 \xi_3 \cos \theta - g_1 \xi_2^3 - g_2(|\xi_1|^2 + |\xi_3|^2)\xi_2, \\
\tau \dfrac{\partial \xi_3}{\partial t} = \mu \xi_3 + h \xi_2 \xi_1 \cos \theta - g_1 \xi_3^3 - g_2(|\xi_1|^2 + |\xi_2|^2)\xi_3,
\end{cases} \tag{26}
$$

with $\theta = \theta_1 + \theta_2 + \theta_3$. Based on the first equation of (26), we can infer that its solution is stable if $\theta = 0$ and $h > 0$ or $\theta = \pi$ and $h < 0$. Consequently, we obtain the following amplitude equations

$$
\begin{cases}
\tau \dfrac{\partial \xi_1}{\partial t} = \mu \xi_1 + |h|\xi_2 \xi_3 - g_1 \xi_1^3 - g_2(|\xi_2|^2 + |\xi_3|^2)\xi_1, \\
\tau \dfrac{\partial \xi_2}{\partial t} = \mu \xi_2 + |h|\xi_1 \xi_3 - g_1 \xi_2^3 - g_2(|\xi_1|^2 + |\xi_3|^2)\xi_2, \\
\tau \dfrac{\partial \xi_3}{\partial t} = \mu \xi_3 + |h|\xi_2 \xi_1 - g_1 \xi_3^3 - g_2(|\xi_1|^2 + |\xi_2|^2)\xi_3.
\end{cases} \tag{27}
$$

By employing the amplitude Eq. (27) and referring to existing literature [7,9,28], we can determine the pattern selection of the reaction–diffusion model (2) as follows.

(i) Spot pattern:

$$
\xi_1 = \xi_2 = \xi_3 = 0,
$$

which is stable when $\mu < \mu_2 = 0$ and unstable when $\mu > \mu_2 = 0$.

(ii) Stripe pattern:

$$
\xi_1 = \sqrt{\frac{\mu}{g_1}} \neq 0, \xi_2 = \xi_3 = 0.
$$

It is stable when $\mu > \mu_3 = \dfrac{h^2 g_1}{(g_2 - g_1)^2}$ and unstable when $\mu < \mu_3$.

(iii) Hexagonal pattern H_0 or H_π when $\theta = 0$ or $\theta = \pi$:

$$
\xi_1 = \xi_2 = \xi_3 = \frac{|h| \pm \sqrt{h^2 + 4(g_1 + 2g_2)\mu}}{2(g_1 + 2g_2)}.
$$

Its existence condition is $\mu > \mu_1 = \dfrac{-h^2}{4(g_1 + 2g_2)}$. Moreover, ξ^+ is stable only for $\mu < \mu_4 = \dfrac{(2g_1 + g_2)h^2}{(g_2 - g_1)^2}$. The solution ξ^- is always unstable, where

$$
\xi^+ = \frac{|h| + \sqrt{h^2 + 4(g_1 + 2g_2)\mu}}{2(g_1 + 2g_2)}, \quad \xi^- = \frac{|h| - \sqrt{h^2 + 4(g_1 + 2g_2)\mu}}{2(g_1 + 2g_2)}.
$$

(iv) Mixed structural state:

$$
\xi_1 = \frac{|h|}{g_2 - g_1}, \ \xi_2 = \xi_3 = \sqrt{\frac{\mu - g_1 \xi_1^2}{g_1 + g_2}},
$$

it exists when $\mu > \mu_3$ and is always unstable with $g_2 > g_1$.

We establish the following conclusion.

Theorem 3.2. *Suppose that $0 < a < 1 + b, 0 < H < 1 - \frac{a}{1+b}$, we have*

(i) the spot solution is stable when $\mu < \mu_2$ and unstable when $\mu > \mu_2$.

(ii) the stripe solution is stable when $\mu > \mu_3$ and unstable when $\mu < \mu_3$.

(iii) the hexagonal solution exists when $\mu > \mu_1$. Moreover, the solution ρ^+ is stable for $\mu < \mu_4$ and ρ^- is always unstable.

(iv) the mixed solution exists and is always unstable when $g_2 > g_1$ and $\mu > \mu_3$.

4. Numerical simulation

4.1. Pattern formation in 2D space

In this subsection, we want to visualize the pattern formation of the diffusive model (2) within a 2D domain, $\Omega = (0, 100) \times (0, 100)$. For discretization of the domain, we consider a uniform spatial grid. Let N be the number of spatial grid points and $h = 100/N$ be the uniform spatial step size. Then, the discrete computational domain is defined as $\Omega_h = \{(x_p, y_q) \mid (p - 0.5)h, (q - 0.5)h, 1 \leq p, q \leq N\}$. Within this discrete computational domain Ω_h, we define the notations for numerical approximations as $u_{pq}^n := u(x_p, y_q, n\Delta t)$ and $w_{pq}^n := w(x_p, y_q, n\Delta t)$, where Δt is a time step size. The continuous model (2) can be discretized using the explicit Euler method as follows:

$$\begin{cases} \dfrac{u_{pq}^{n+1} - u_{pq}^n}{\Delta t} = d_1 \Delta_h u_{pq}^n + u_{pq}^n(1 - u_{pq}^n) - \dfrac{a(u_{pq}^n)^2 w_{pq}^n}{(u_{pq}^n)^2 + b(w_{pq}^n)^2} - H u_{pq}^n, \\ \dfrac{w_{pq}^{n+1} - w_{pq}^n}{\Delta t} = d_2 \Delta_h w_{pq}^n + \gamma w_{pq}^n \left(1 - \dfrac{w_{pq}^n}{u_{pq}^n}\right), \end{cases} \quad (28)$$

where

$$\Delta_h u_{pq} = \frac{u_{p+1,q} + u_{p-1,q} + u_{p,q+1} + u_{p,q-1} - 4u_{pq}}{h^2}$$

and

$$\Delta_h w_{pq} = \frac{w_{p+1,q} + w_{p-1,q} + w_{p,q+1} + w_{p,q-1} - 4w_{pq}}{h^2}.$$

From Eq. (28), we can obtain the numerical solutions with the previous time solutions u^n and w^n as follows:

$$\begin{cases} u_{pq}^{n+1} = u_{pq}^n + \Delta t \left[d_1 \Delta_h u_{pq}^n + u_{pq}^n(1 - u_{pq}^n) - \dfrac{a(u_{pq}^n)^2 w_{pq}^n}{(u_{pq}^n)^2 + b(w_{pq}^n)^2} - H u_{pq}^n \right], \\ w_{pq}^{n+1} = w_{pq}^n + \Delta t \left[d_2 \Delta_h w_{pq}^n + \gamma w_{pq}^n \left(1 - \dfrac{w_{pq}^n}{u_{pq}^n}\right) \right]. \end{cases}$$

For the following numerical simulation, the time step size is set to be $\Delta t = 0.01$, and the spatial step length is $h = 1$. The initial conditions are given as follows:

$$\begin{cases} u(x, y, 0) = u_* + 0.01\xi_*(x, y), \\ w(x, y, 0) = w_* + 0.01\xi_*(x, y), \end{cases} \quad (29)$$

where $\xi_*(x, y)$ is the uniformly distributed random perturbation between -1 and 1. In the following, we only display the pattern of the solution $u(x, y, t)$ because a similar pattern can be observed for the solution $w(x, y, t)$.

First, we choose the parameters $a = 0.78, b = 0.25, \gamma = 0.35, d_1 = 0.2, d_2 = 2.5$, and $H = 0.235$ for the model (2). This choice results in $E_* = (u_*, w_*) = (0.1410, 0.1410)$, $H_0 + \gamma = 0.3516$, and $(\gamma d_1 + H_0 d_2)^2 - 4d_1 d_2 D_0 = -0.0932 < 0$. Therefore, statement (ii) of Theorem 3.1 implies that there exists a unique potential critical value of the Turing instability $H_c = H_3^c = 0.1553$. Obviously, the assumption $H_0 + \gamma > H > H_3^c$ is valid in statement (ii) of Theorem 3.1 and thereby, the model (2) admits pattern formation due to the existence of the Turing instability. On the other hand, we obtain the following results: $\phi = 4.1218, \varphi = -0.4873, h_1 = 1.9880, h_2 = -24.2190, u_{00} = 252.4896, w_{00} = 114.2496, u_{11} = 33.8917, w_{11} = -3.5312, u_{22} = 128.1578, w_{22} = -1.3039, c_1 = -1.7290e + 03, c_2 = -2.8910e + 03, c_3 = -600.9055, c_4 = 94.2379$. As a result, we obtain $g_1 = 2.2441e + 03, g_2 = 4.5891e + 03, h = 43.0560, \mu = 0.5135, \mu_1 = -0.0406, \mu_2 = 0, \mu_3 = 0.7565$, and $\mu_4 = 3.0602$. Hence,

we can ensure that $\mu_1 < \mu_2 < \mu < \mu_3 < \mu_4$ is valid. Our numerical experiment illustrates that the emergence of hexagonal patterns in the model (2), as shown in Fig. 4. As a consequence, statement (iii) of Theorem 3.2 is confirmed to be true.

Next, let us keep the parameters $a = 0.78, b = 0.25, \gamma = 0.35, d_1 = 0.2, d_2 = 2.5$, and $H = 0.21$ in the model (2). As a consequence, we obtain the unique positive equilibrium $E_* = (u_*, w_*) = (0.1660, 0.1660)$, $H_0 + \gamma = 0.3516$, and $(\gamma d_1 + H_0 d_2)^2 - 4d_1 d_2 D_0 = -0.1107 < 0$. Therefore, by using statement (ii) of Theorem 3.1, we know that there exists a unique potential critical value of the Turing instability $H_c = H_3^c = 0.1660$. Obviously, the assumption $H_0 + \gamma > H > H_3^c$ is valid in statement (ii) of Theorem 3.1. This implies that there is pattern formation owing to the existence of the Turing instability. Furthermore, we can compute the following values: $\phi = 3.8929, \varphi = -0.4006, h_1 = -1.3128, h_2 = -17.6446, u_{00} = 167.2181, w_{00} = 66.3916, u_{11} = 3.1049, w_{11} = -4.4051, u_{22} = 22.5185, w_{22} = -9.4295, c_1 = -1.1711e + 03, c_2 = -1.9700e + 03, c_3 = -80.2238, c_4 = 863.0119$. Thereby, we obtain $g_1 = 1.7629e + 03, g_2 = 3.5847e + 03, h = 17.8205, \mu = 0.2654, \mu_1 = -0.0089, \mu_2 = 0, \mu_3 = 0.1687$, and $\mu_4 = 0.6804$. Clearly, $\mu_1 < \mu_2 < \mu_3 < \mu < \mu_4$ is valid. By employing statement (iv) of Theorem 3.2, we infer that there are mixed patterns in the model (2). The numerical simulation results show that there are spot and stripe patterns can coexist in the bounded domain, as shown in Fig. 5. Consequently, our theoretical prediction is valid.

4.2. Pattern formation on the spherical and torus surfaces

4.2.1. Discretization of the Laplace–beltrami operator on a triangular surface mesh

To simulate pattern formation on curved surfaces such as spheres and tori using the harvested predator–prey model, let us consider the Laplace–Beltrami operator Δ_S on a closed, smooth curved surface S. The Laplace–Beltrami operator can be discretized on triangular surface mesh using simple and explicit methods [36,37]. Let S_d be a triangulated surface mesh with v vertex points as shown in Fig. 6(a). The set of given surface points on the triangulated surface mesh S_d is labeled by $\{\mathbf{x}_i\}_{i=1}^v = \{\mathbf{x}_1, \mathbf{x}_2, \mathbf{x}_3, \ldots, \mathbf{x}_v\}$. On the triangulated curved surface S_d, for surface points $\mathbf{x}_i$, we denote the numerical solutions by $u_i^n := u(\mathbf{x}_i, n\Delta t)$ and $w_i^n := w(\mathbf{x}_i, n\Delta t)$, where Δt is the time step.

We can discretize the model (2) by using the explicit Euler method with the discretized Laplace–Beltrami operator Δ_S on triangulated curved surfaces:

$$\begin{cases} \dfrac{u_i^{n+1} - u_i^n}{\Delta t} = d_1 \Delta_S u_i^n + u_i^n(1 - u_i^n) - \dfrac{a(u_i^n)^2 w_i^n}{(u_i^n)^2 + b(w_i^n)^2} - H u_i^n, \\ \dfrac{w_i^{n+1} - w_i^n}{\Delta t} = d_2 \Delta_S w_i^n + \gamma w_i^n \left(1 - \dfrac{w_i^n}{u_i^n}\right), \quad \text{for } i = 1, \ldots, v. \end{cases}$$

Therefore, we can obtain the numerical solutions using the previous time solutions u^n and w^n as follows:

$$\begin{cases} u_i^{n+1} = u_i^n + \Delta t \left[d_1 \Delta_S u_i^n + u_i^n(1 - u_i^n) - \dfrac{a(u_i^n)^2 w_i^n}{(u_i^n)^2 + b(w_i^n)^2} - H u_i^n \right], \\ w_i^{n+1} = w_i^n + \Delta t \left[d_2 \Delta_S w_i^n + \gamma w_i^n \left(1 - \dfrac{w_i^n}{u_i^n}\right) \right]. \end{cases}$$

For a given surface point $\mathbf{x}_i$ in the triangular surface mesh S_d, the set of surrounding one-ring triangular surface point indices is defined as $I(i) = \{i_1, i_2, \ldots, i_m\}$, where $i_1 = i_m$, as shown in Fig. 6(b). Then, the discretized Laplace–Beltrami operator at surface point $\mathbf{x}_i$ can be defined as follows:

$$\begin{cases} \Delta_S u_i = \dfrac{3}{\mathcal{A}(\mathbf{x}_i)} \displaystyle\sum_{j \in I(i)} \dfrac{\cot \alpha_{ij} + \cot \beta_{ij}}{2}(u_j - u_i), \\ \Delta_S w_i = \dfrac{3}{\mathcal{A}(\mathbf{x}_i)} \displaystyle\sum_{j \in I(i)} \dfrac{\cot \alpha_{ij} + \cot \beta_{ij}}{2}(w_j - w_i), \end{cases}$$

M. Chen et al.

Chaos, Solitons and Fractals: the interdisciplinary journal of Nonlinear Science, and Nonequilibrium and Complex Phenomena 176 (2023) 114153
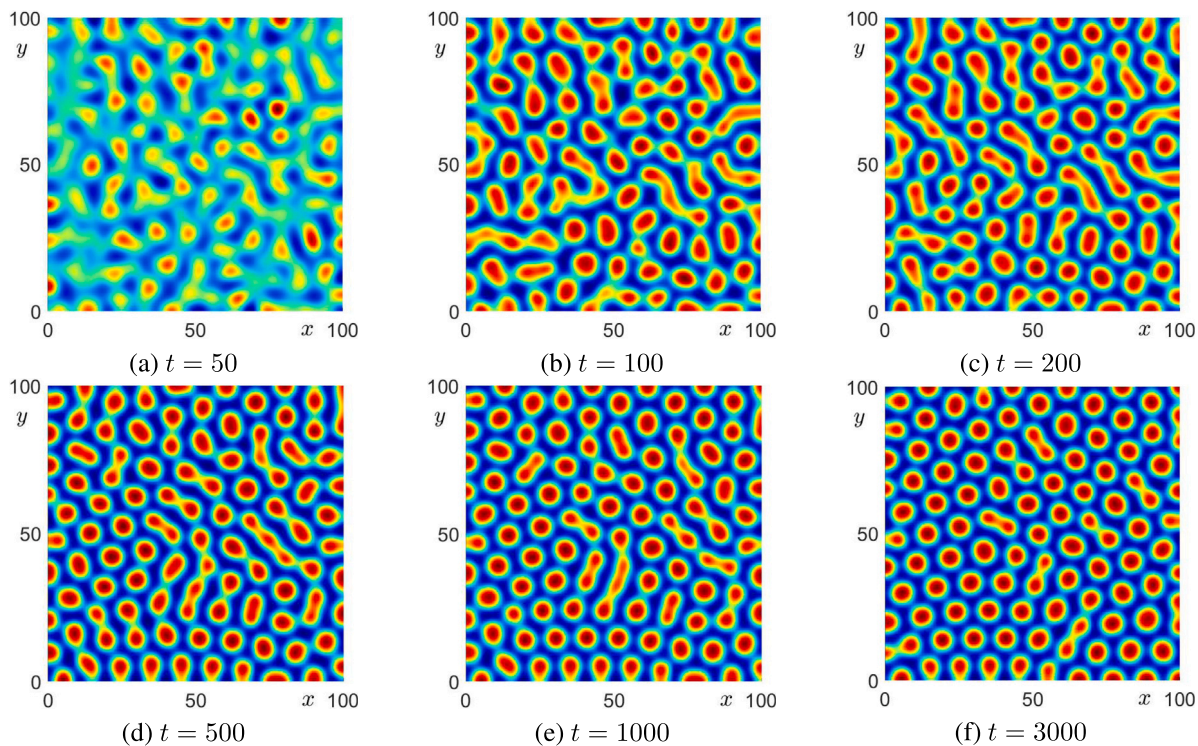
Fig. 4. Time evolution pictures of the hexagonal pattern. Here, we choose the parameter values: $a = 0.78, b = 0.25, \gamma = 0.35, d_1 = 0.2, d_2 = 2.5$, and $H = 0.235$.
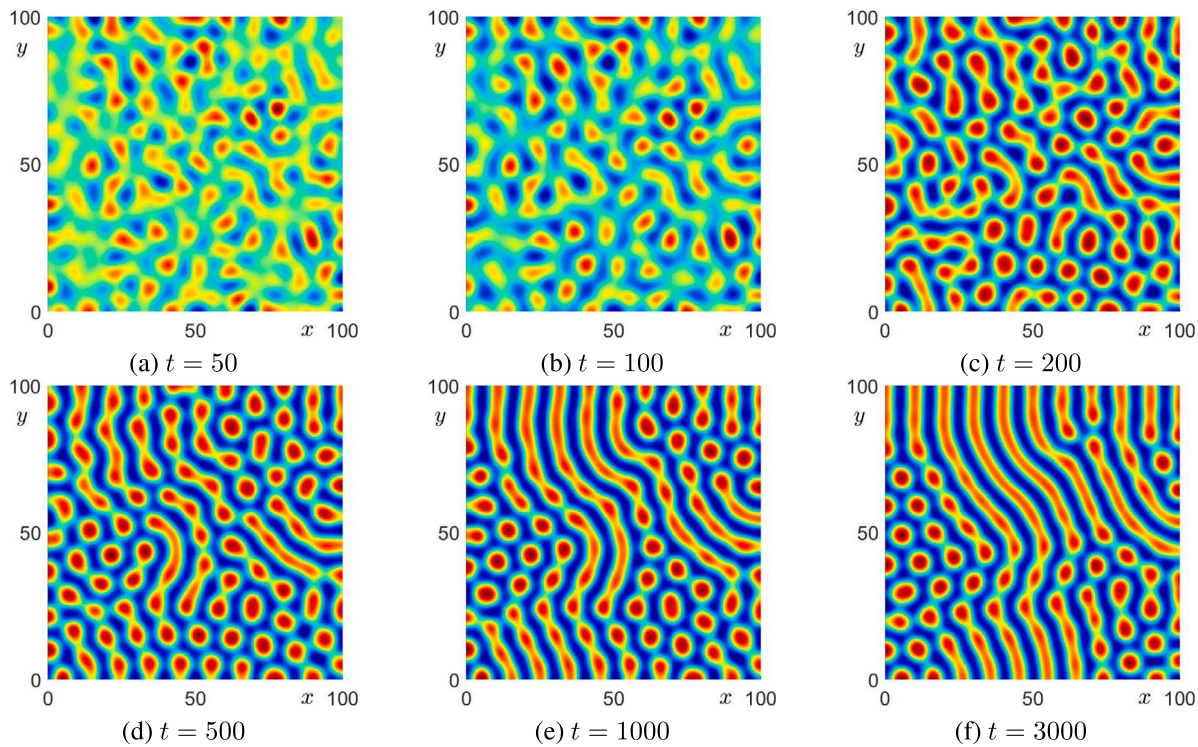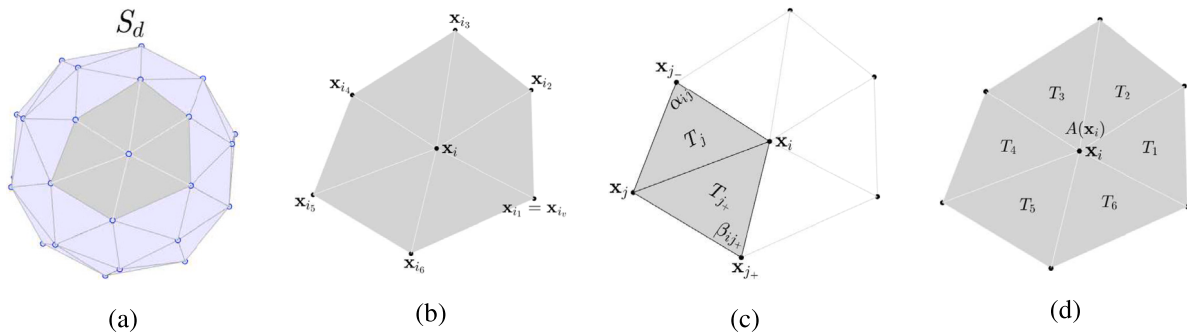

Fig. 5. Time evolution pictures of the mixed pattern. Here, we choose the parameter values: $a = 0.78, b = 0.25, \gamma = 0.35, d_1 = 0.2, d_2 = 2.5$, and $H = 0.21$.

Fig. 6. Visual schematic illustrations: (a) triangular surface mesh, (b) surrounding one-ring surface points set for $\mathbf{x}_i$, (c) triangles T_j and T_{j+} featuring the angles α_{ij} and β_{ij_+} and (d) vertex $\mathbf{x}_i$ and its corresponding area $\mathcal{A}(\mathbf{x}_i)$.

where α_{ij} and β_{ij} are angles in triangles T_j and T_{j+}, respectively, as shown in Fig. 6(c) [38]. The area enclosed by the one-ring points of the vertex $\mathbf{x}_i$, as shown in Fig. 6(d), is defined as follows:

$$\mathcal{A}(\mathbf{x}_i) = \sum_{j \in I(i)} \frac{\sqrt{\|\mathbf{x}_j - \mathbf{x}_i\|^2 \|\mathbf{x}_{j_+} - \mathbf{x}_i\|^2 - \left(\mathbf{x}_j - \mathbf{x}_i, \mathbf{x}_{j_+} - \mathbf{x}_i\right)^2}}{2}.$$

To simulate pattern formation on the discrete surfaces, such as spheres and tori, using the discretized harvested predator–prey model and the above-mentioned explicit time-stepping approach, we conduct numerical experiments with the following initial conditions:

$$\begin{cases} u(\mathbf{x}_i, 0) = u_* + 0.01\xi_*(\mathbf{x}_i), \\ w(\mathbf{x}_i, 0) = w_* + 0.01\xi_*(\mathbf{x}_i), \end{cases} \tag{30}$$

where $\xi_*(\mathbf{x}_i)$ is the uniformly distributed random perturbation between -1 and 1.

4.2.2. Pattern formation on the spherical surface

First, let us choose the parameters $a = 0.78, b = 0.25, \gamma = 0.35, d_1 = 0.2, d_2 = 2.5$, and $H = 0.235$ in the model (2). The triangulated spherical surface mesh S_d has a radius value of $r = 50$, and it consists of $v = 11856$ triangulated spherical surface points.

As shown in Fig. 7, we present the temporal evolution of behaviors on the surface of the harvested predator–prey system with a harvesting coefficient of $H = 0.235$. It demonstrates that spotted patterns fill the spherical surfaces. Next, we consider the parameter values $a = 0.78, b = 0.25, \gamma = 0.35, d_1 = 0.2, d_2 = 2.5$, and a harvesting coefficient of $H = 0.21$ in the predator–prey model (2). In the numerical results on triangulated spherical surfaces, as the value of the harvesting coefficient H approaches 0.21, the frequency of appearance of the stripe patterns increases, and these stripe patterns form along the great circles of the spherical surface as shown in Fig. 8. In this case, the stripe and spot patterns on the spherical surface appear. The initial data used here is Eq. (30).

4.2.3. Pattern formation on the tours surface

Let us display the pattern formation of the diffusive model (2) on a triangular surface with a different topological structure from a spherical surface, such as a torus. Accordingly, the following numerical experiments will show the pattern formation on a triangulated surface mesh T_d of a torus. The torus has a major radius (the length from the center of the torus to the center of the tube) value of $R = 50$, a minor radius (generating circle) value of $r = 20$, and the number of triangulated torus surface points is $v = 14272$. We use the same initial conditions as mentioned above, while keeping the parameters $a = 0.78, b = 0.25, \gamma = 0.35, d_1 = 0.2, d_2 = 2.5$, and $H = 0.235$ in the model (2). As shown in Fig. 9, the formation of spot patterns emerges on a triangulated torus as time, represented by the variable t, progresses.

On the other hand, if we assume that $a = 0.78, b = 0.25, \gamma = 0.35, d_1 = 0.2, d_2 = 2.5$, and $H = 0.21$ in the model (2), then both stripe

patterns and spot patterns appear on the surface of the torus, as shown in Fig. 10.

4.3. Effect of the diffusion rate d_1

In ecological systems, generally, the diffusion rates of prey and predator species play a significant role in pattern formation. To investigate this, we will fix the parameters as used in Fig. 8 constant and only vary the value of the diffusion rate d_1 of the prey species. The corresponding patterns can be found in Fig. 11. Precisely, when we take $d_1 = 0.05$, we observe pattern formation with irregular shapes, as shown in (a). As we increase d_1 to $d_1 = 0.1$, a mixture of stripe and spot patterns emerges, see figure (b). This pattern mixture persists when we choose $d_1 = 0.15$ and $d_1 = 0.2$ in figures (c) and (d), respectively. If we choose $d_1 = 0.25$ in figure (e), then it is clear that there are few stripe patterns format on the spherical surface, and the spot patterns occupy the majority of the spherical surface. However, as we further increase d_1 of the prey species, i.e., $d_1 = 0.3$, both the stripe and spot patterns completely disappear, as shown in Fig. 11(f). This observation suggests that the diffusion rate has a significant influence on the pattern formation in the diffusive predator–prey model (2). Biologically, small movement of the prey species can lead to spatial self-organization in the predator–prey model (2), while a higher diffusion rate of the prey population results in a stable homogeneous state. This phenomenon may provide a helpful reference to understand the interaction dynamics between the prey and predator species.

In conclusion, we confirm the validity of our theoretical analysis. We observe spatial pattern formation in the diffusive model (2) in a 2D space, on a spherical surface, and on a torus surface by considering the harvesting coefficient H as the Turing instability parameter. Different patterns can be displayed as we vary the harvesting coefficient H. From the ecological point of view, the distributions of the prey's and predator's densities admit spot and mixed forms in a bounded domain or surface; meanwhile, the spot patterns and mixed patterns in Figs. 4 and 5,7–10 imply that the densities of the prey and predator populations will achieve their maximum. However, the blue parts in 2D space and on the spherical and torus surfaces suggest that the densities of the prey and predator species have minimum values. Obviously, the change of the harvesting coefficient of the prey species will lead to different shapes of the patterns, namely, harvesting has an increasing influence on the final density of the prey and predator populations. Therefore, it is possible to control the predator–prey system such that the system performs different dynamic patterns by adjusting the harvesting rate of the prey species. As a result, we can theoretically and numerically predict the influence of the harvesting effect and it can be regarded as an important mechanism for the appearance of complicated spatial dynamics in ecological models. Meanwhile, we can observe that the diffusion rate of the prey species will strongly affect the pattern formation of the model (2), as shown in Fig. 11. These findings highlight the complex dynamics of the prey–predator interaction, showing how suitable changes of the harvesting parameter and diffusion rate can lead to significant shifts in the system's dynamical behaviors.
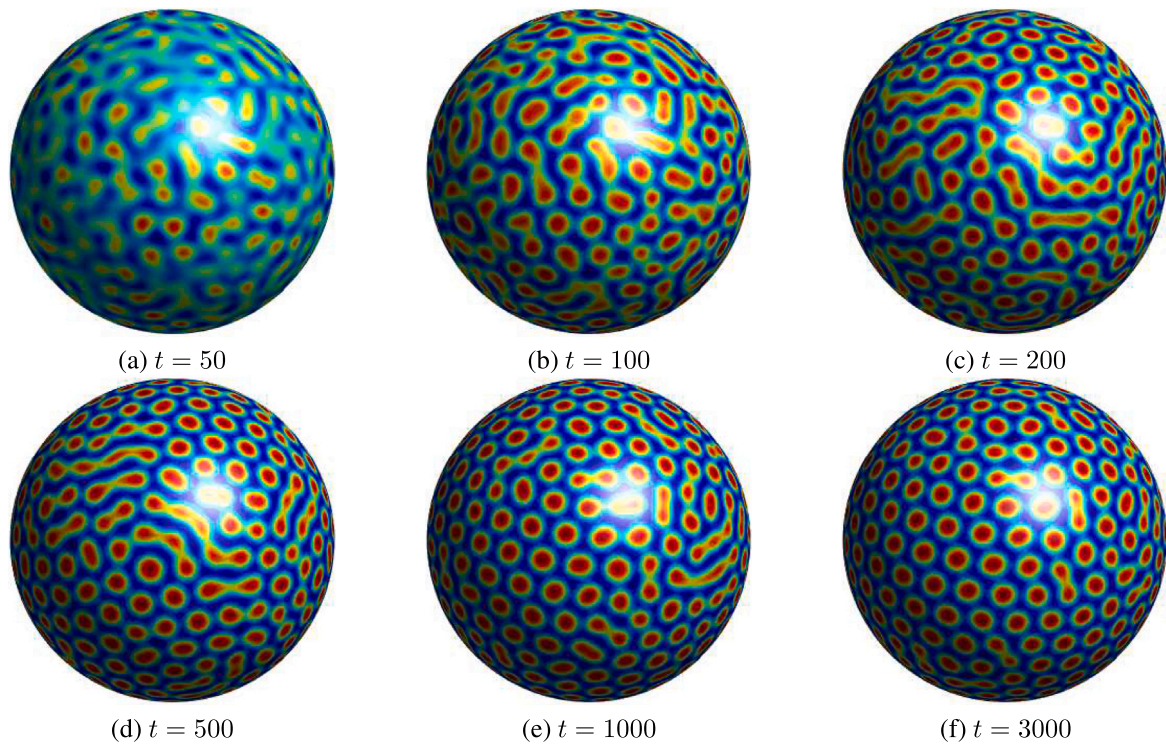
(a) $t = 50$

(b) $t = 100$

(c) $t = 200$

(d) $t = 500$

(e) $t = 1000$

(f) $t = 3000$

Fig. 7. Pattern formations of prey u on a triangulated spherical surface. The parameters used are $\Delta t = 0.01, a = 0.78, b = 0.25, \gamma = 0.35, d_1 = 0.2, d_2 = 2.5$, and the harvesting coefficient $H = 0.235$.
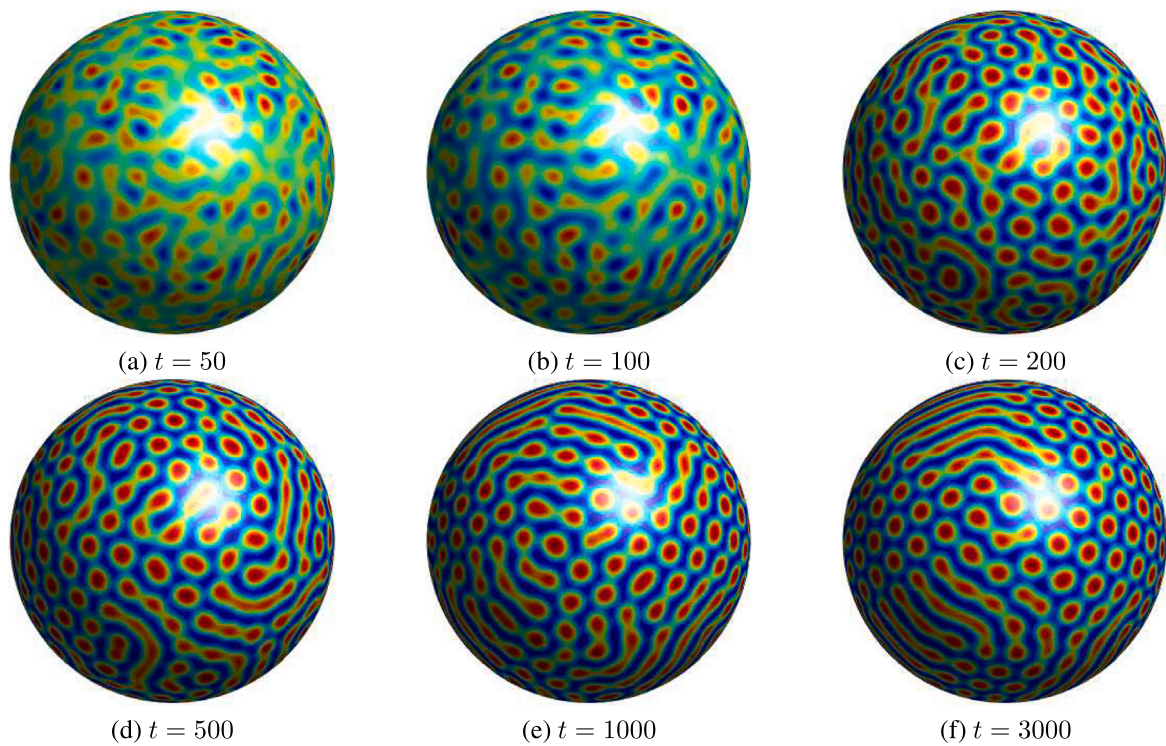

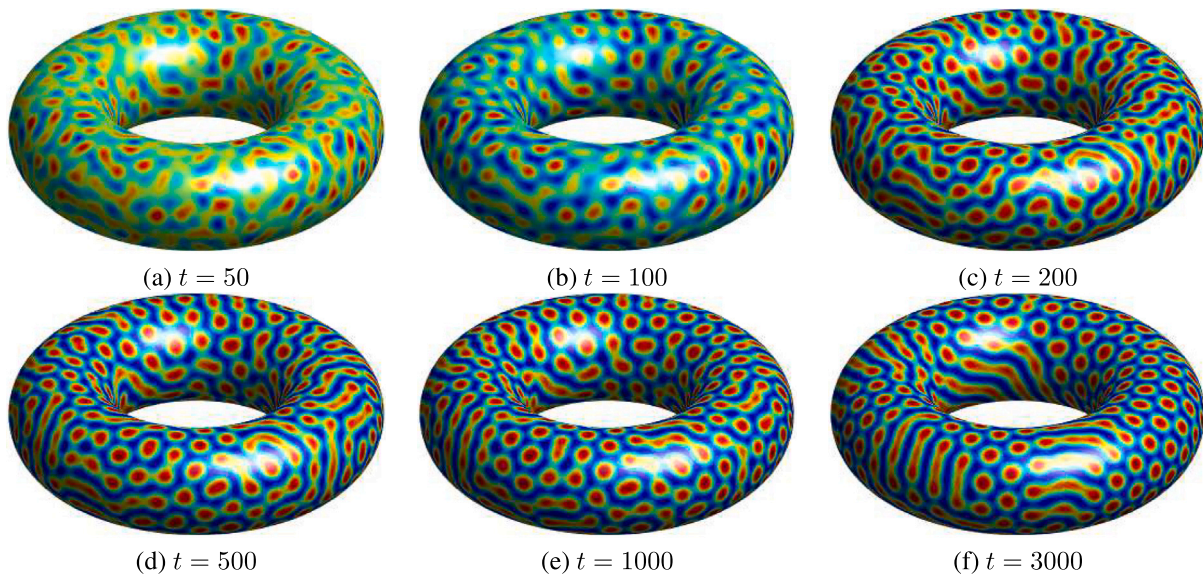(a) $t = 50$

(b) $t = 100$

(c) $t = 200$

(d) $t = 500$

(e) $t = 1000$

(f) $t = 3000$

Fig. 8. Pattern formations of prey u on a triangulated spherical surface. The parameters used are $\Delta t = 0.01, a = 0.78, b = 0.25, \gamma = 0.35, d_1 = 0.2, d_2 = 2.5$, and the harvesting coefficient $H = 0.21$.

| (a) $t = 50$ | (b) $t = 100$ | (c) $t = 200$ |
| (d) $t = 500$ | (e) $t = 1000$ | (f) $t = 3000$ |

Fig. 9. Pattern formations of prey u on a triangulated torus. The parameters used are $\Delta t = 0.01, a = 0.78, b = 0.25, \gamma = 0.35, d_1 = 0.2, d_2 = 2.5$, and the harvesting coefficient $H = 0.235$.

| (a) $t = 50$ | (b) $t = 100$ | (c) $t = 200$ |
| (d) $t = 500$ | (e) $t = 1000$ | (f) $t = 3000$ |
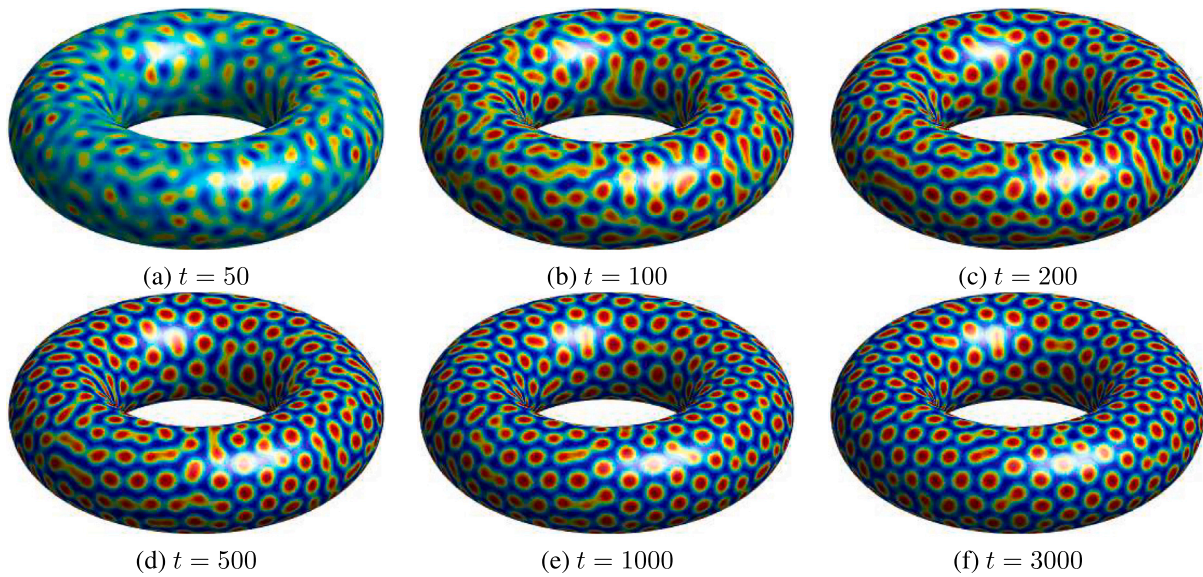
Fig. 10. Pattern formations of prey u on a triangulated torus. The parameters used are $\Delta t = 0.01, a = 0.78, b = 0.25, \gamma = 0.35, d_1 = 0.2, d_2 = 2.5$, and the harvesting coefficient $H = 0.21$.

5. Conclusions

Harvesting is a common phenomenon in the real world due to commercial interests or for maintaining ecological balance. In this paper, we reported the pattern dynamics of a predator–prey model with the harvesting term in the prey species. Owing to the pattern caused by Turing instability, we first investigated the stability of the positive equilibrium for the local temporal model. It was found that the positive equilibrium E_* undergoes "stable node → stable focus→ unstable focus → unstable node" and center with the change of the harvesting constant H, see Theorem 2.1. Moreover, we analyzed the occurrence of supercritical and subcritical Hopf bifurcation near the center using the first Lyapunov number, see Theorem 2.2. For the diffusive model, we

explored the stability of the positive equilibrium E_* and the existence of Turing instability by choosing the harvesting coefficient H as the critical parameter, see Theorem 3.1. To determine the spatial pattern selection around the Turing instability onset $H = H_c$, we employed the weakly nonlinear analysis method to deduce the amplitude equation, which revealed various spatial patterns, see Theorem 3.2. Finally, we conducted numerical experiments to validate our theoretical results for different values of the harvesting coefficient H, see Figs. 4–5 and Figs. 7–10. Especially, these patterns can be formed on spherical and tours surfaces. Overall, we explored the rich dynamic behaviors of this predator–prey model with the harvesting term. We found that the harvesting plays a crucial role in governing the existence of Hopf bifurcation and Turing instability, and the pattern structure changes with adjustments in the parameter range of the harvesting constant H.
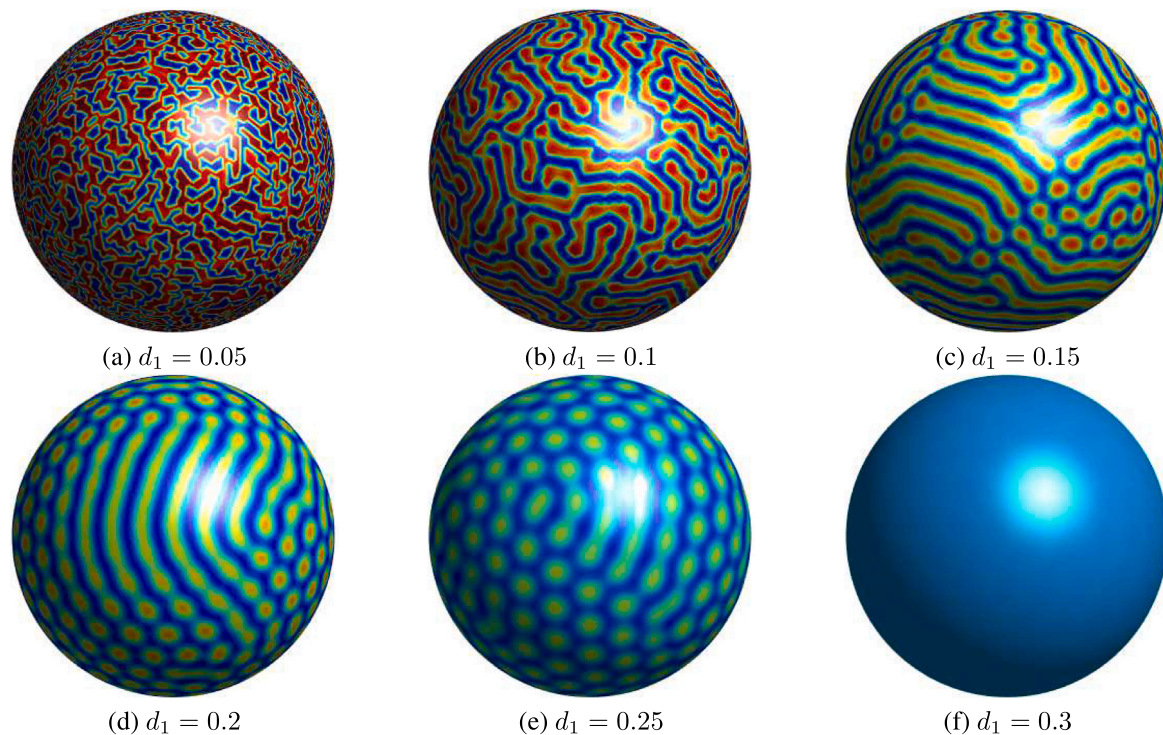
Fig. 11. Pattern formations of prey u on a spherical surface at $t = 3000$. The parameters used are $\Delta t = 0.01, a = 0.78, b = 0.25, \gamma = 0.35, d_2 = 2.5$, and the harvesting coefficient $H = 0.21$.

We look forward to reporting more interesting results of this model in upcoming works.

CRediT authorship contribution statement

Mengxin Chen: Formal analysis, Writing – original draft, Review & editing, Project administration. **Seokjun Ham:** Formal analysis, Writing – original draft, Numerical computation. **Yongho Choi:** Methodology, Codes design, Review & editing, Numerical computation. **Hyundong Kim:** Codes design, Review & editing, Numerical computation. **Junseok Kim:** Supervision, Methodology, Software, Numerical computation, Review & editing, Project administration.

Declaration of competing interest

The authors declare that they have no known competing financial interests or personal relationships that could have appeared to influence the work reported in this paper.

Data availability

No data was used for the research described in the article.

Acknowledgments

References

[1] Turing AM. The chemical basis of morphogenesis. Philos Trans R Soc Lond Ser B: Biol Sci 1952;237:37–72.

[2] Li Y, Zhou Y. Turing–Hopf bifurcation in a general Selkov-Schnakenberg reaction–diffusion system. Chaos Solit Fract 2023;171:113473.

[3] Han R, Mandal G, Guin LN, Chakravarty S. Dynamical response of a reaction–diffusion predator–prey system with cooperative hunting and prey refuge. J Stat Mech 2022;2022:103502.

[4] Sarker RC, Sahani SK. Turing pattern dynamics in an SI epidemic model with superdiffusion. Int J Bifurcation Chaos 2022;32:2230025.

[5] Dolnik M, Konow C, Somberg NH, Epstein IR. Effect of obstructions on growing Turing patterns. Chaos 2022;32:073127.

[6] Chang LL, Liu C, Sun GQ, Wang Z, Jin Z. Delay-induced patterns in a predator–prey model on complex networks with diffusion. New J Phys 2019;21:073035.

[7] Chen MX, Wu RC, Chen LP. Pattern dynamics in a diffusive Gierer-Meinhardt model. Int J Bifurcation Chaos 2020;30(12):2030035.

[8] Liu Y, Maini PK, Baker RE. Control of diffusion-driven pattern formation behind a wave of competency. Physica D 2022;438:133297.

[9] Banerjee M, Ghorai S, Mukherjee N. Study of cross-diffusion induced Turing patterns in a ratio-dependent predator–prey model via amplitude equations. Appl Math Model 2018;55:383–99.

[10] Kondo S, Watanabe M, Miyazawa S. Studies of Turing pattern formation in Zebrafish skin. Philos Trans R Soc A 2021;379:20200274.

[11] Chen MX, Wu RC. Steady states and spatiotemporal evolution of a diffusive predator–prey model. Chaos Solit Fract 2023;170:113397.

[12] Chen MX, Srivastava HM. Stability of bifurcating solution of a predator–prey model. Chaos Solit Fract 2023;168:113153.

[13] Han RJ, Guin LN, Acharya S. Complex dynamics in a reaction-cross-diffusion model with refuge depending on predator–prey encounters. Eur Phys J Plus 2022;137:134.

[14] Guin LN, Pal S, Chakravarty S, Djilali S. Pattern dynamics of a reaction–diffusion predator–prey system with both refuge and harvesting. Int J Biomath 2021;14:2050084.

[15] Han R, Guin LN, Dai B. Consequences of refuge and diffusion in a spatiotemporal predator–prey model. Nonlinear Anal-Real World Appl 2021;60:103311.

[16] Holling CS. The functional response of predator to prey density and its role in mimicry and population regulation. Men Ent Sec Can 1965;45:1–60.

[17] Leslie PH, Gower JC. The properties of a stochastic model for the predator–prey type of interaction between two species. Biometrika 1960;47:219–34.

[18] Bhattacharyya J, Chatterjee A. Dynamics of a fishery model with continuous threshold harvesting policy and its leverage for conservation and management. J Biol Syst 2022;30:913–43.

[19] Al-Omari J, Gumah G, Al-Omari S. Dynamics of a harvested stage-structured predator–prey model with distributed maturation delay. Math Methods Appl Sci 2022;45:761–9.

[20] Jiang ZC, Zhang WZ, Zhang J, Zhang T. Dynamical analysis of a phytoplankton-zooplankton system with harvesting term and Holling III functional response. Int J Bifurcation Chaos 2018;28:1850162.

[21] Xiao DM. Dyanmics and bifurcations on a class of population model with seasonal constant-yield harvesting. Discret Contin Dyn Syst B 2016;21:699–719.

[22] Zhang FR, Zhang XH, Li Y, Li C. Hopf bifurcation of a delayed predator–prey model with nonconstant death rate and constant-rate prey harvesting. Int J Bifurcation Chaos 2018;28:1850179.

[23] Yao Y. Bifurcations of a Leslie–Gower prey-predator system with ratio-dependent Holling IV functional response and prey harvesting. Math Methods Appl Sci 2020;43:2137–70.

[24] Chen MX, Wu RC. Patterns in the predator–prey model with network connection and harvesting policy. Math Methods Appl Sci 2023;46(2):2433–54.

[25] Guin LN, Acharya S. Dynamic behaviour of a reaction–diffusion predator–prey model with both refuge and harvesting. Nonlinear Dynam 2017;88:1501–33.

[26] Gupta RP, Chandra P. Dynamical properties of a prey-predator-scavenger model with quadratic harvesting. Commun Nonlinear Sci Numer Simul 2017;49:202–14.

[27] Sharma A, Sharma AK, Agnihotri K. Complex dynamic of plankton-fish inter-action with quadratic harvesting and time delay. Model Earth Syst Environ 2016;2:204.

[28] Chen MX, Wu RC, Liu B, Chen L. Pattern selection in a predator–prey model with Michaelis–Menten type nonlinear predator harvesting. Ecol Complex 2018;36:239–49.

[29] Yan XP, Zhang CH. Global stability of a delayed diffusive predator–prey model with prey harvesting of Michaelis–Menten type. Appl Math Lett 2021;114:106904.

[30] Wang Y, Zhou X, Jiang W. Bifurcations in a diffusive predator–prey system with linear harvesting. Chaos Solit Fract 2023;169:113286.

[31] Clark CW. Aggregation and fishery dynamics: A theoretical study of schooling and the purse seine tuna fisheries. Fish Bull 1979;77(2):317–37.

[32] Chen MX, Wu RC, Chen LP. Spatiotemporal patterns induced by Turing and Turing–Hopf bifurcation in a predator–prey system. Appl Math Comput 2020;380:125300.

[33] Shi HB, Li Y. Global asymptotic stability of a diffusive predator–prey model with ratio-dependent functional response. Appl Math Comput 2015;250:71–7.

[34] Chen MX, Wu RC, Liu HX, Fu X. Spatiotemporal complexity in a Leslie–Gower type predator–prey model near Turing–Hopf point. Chaos Solit Fract 2021;153:111509.

[35] Perko L. Differential equations and dynamical systems. New York: Springer-Verlag; 2001.

[36] Desbrun M, Meyer M, Schroder P, Barr A. Implicit fairing of irregular meshes using diffusion and curvature flow. In: Proceedings of the 26th annual conference on Computer graphics and interactive techniques. 1999.

[37] Kim H, Yun A, Yoon S, Lee C, Park J, Kim J. Pattern formation in reaction–diffusion systems on evolving surfaces. Comput Math Appl 2020;80(9):2019–28.

[38] Meyer M, Desbrun M, Schröder P, Barr AH. Discrete differential-geometry operators for triangulated 2-manifolds. In: Visualization and mathematics, vol. 3. 2003, p. 35–57.